# CHARACTERIZING MATERIAL PROPERTIES OF DRAWN MONOFILAMENT FOR TWISTED POLYMER ACTUATION

By Diego R. Higueras Ruiz

A Thesis Submitted in Partial Fulfillment
of the Requirements for the Degree of
Master of Science
in Engineering

Northern Arizona University
August 2018

Approved:
Michael W. Shafer, Ph.D., Chair
Heidi Feigenbaum, Ph.D.
Timothy A. Becker, Ph.D.

# ABSTRACT

# CHARACTERIZING MATERIAL PROPERTIES OF DRAWN MONOFILAMENT FOR TWISTED POLYMER ACTUATION

Diego R. Higueras Ruiz

The field of smart materials has experienced a significant growth in the past fifteen years in actuation applications due to their smart and adaptive capabilities. However, most of these smart materials share the drawback of high cost, making their development and implementation difficult. This limitation leads us to the study of Twisted Polymer Actuators (TPAs). TPAs are inexpensive drawn monofilaments of polymers, such as fishing line, capable of actuation under thermal loads. The actuation on TPAs is due to the anisotropic thermal expansion responses of the material in the radial and axial directions. The properties of the precursor monofilament can be used to predict the actuation of TPAs. This thesis focuses on characterizing the mechanical and thermal properties of the precursor monofilament necessary as input parameters for actuation models. The properties obtained in this thesis are: axial modulus, shear modulus, radial modulus, Poisson's ratio, axial thermal contraction, and radial thermal expansion. The mechanical properties are presented as a function of temperature under the assumption of linear elasticity, but also as a function of time to characterize the viscoelastic effect at room temperature. The thermal expansion properties are also presented as functions of temperature and time, and it is found that viscous effects on thermal properties can be ignored for rapid actuation periods. Finally, this thesis presents experimental actuation data for different test conditions: free torsional actuation and torsional actuation under an isotonic torsional load. In the latter, actuation is performed for two different configurations: single monofilament and a triple strand in parallel arrangement.

# Acknowledgements

First and foremost, I would like to express my gratitude to my advisors Dr. Michael W. Shafer and Dr. Heidi P. Feigenbaum for their dedicated involvement throughout this master thesis research. Without their assistance and support, this thesis would have never been accomplished. I would also like to be thankful to Dr. Becker for taking the time to read my thesis and contribute with improvements. I would like to show my appreciation to Dr. Acker for giving me the opportunity to pursuit my M.S. program at Northern Arizona University. I am very thankful to my labmate, Amy M. Swartz for teaching me how to develop critical and professional writing, as well as contributing to this research with her hardworking and proactive attitude. Last but not least, I am very thankful to my family for teaching me to never give in to the difficulties in the process of achieving my goals and my friends for giving me their entire and unconditional support during the hard times.

# Contents

# List of Tables

# List of Figures

## Chapter 1

# Introduction

### 1.1 Motivation

Actuators normally consist of a set of components built in a specific configuration, along with a control feedback system and source of energy. Electro-mechanical actuators can be voluminous and mechanically complex, characteristics that can potentially limit their scope of applications. The complexity of traditional actuators has led engineers to search for solid-state actuators as a new source of actuation. Some examples include Lead Zirconate Titanate Piezoelectric Ceramics (PZTs), Electroactive Polymers (EAPs), Shape Memory Alloys (SMAs), Magnetic Shape Memory Alloys (MSMAs), Shape Memory Polymers (SMPs), Carbon Nanotubes (CNTs), and Twisted Polymer Actuators (TPAs). These smart materials have been shown to operate as actuators in many fields, including bioengineering, robotics, and aeronautic [5, 6, 7, 1].

Haines et al. [1] showed that drawn polymer monofilaments, such as fishing line, have the ability to operate as linear and torsional actuators under specific twisted and/or coiled configurations, similar to other smart materials [5, 8, 9, 10]; however, twisted polymer actuators stand out from others for being an inexpensive smart material with high specific work capacity under thermal driving loads [1].

To create a torsional polymer actuator, a.k.a. straight twisted polymer actuator (STPA), the precursor monofilament, which is a drawn polymer with straight orientation of the internal fibers, is twisted over its axial axis but the sample still remains straight. After the twisted configuration is reached, the sample is annealed to release internal stresses and fixed to this new orientation of the internal fibers. In this configuration, the internal fibers tend to untwist during heating due to its anisotropic thermal properties. A STPA is displayed in Figure 1.1(a) where the internal fiber is shown in its new orientation. Linear polymer actuators, a.k.a. twisted coiled polymer actuators (TCPAs) are fabricated by inserting twists in the precursor monofilament until the precursor monofilament starts coiling and a spring-shape is yielded (Figure 1.1(b)). After the coiled configuration is reached, the TCPA is constrained in torque at the ends of the sample and a tensile load is normally set at one end. When an increment in temperature is applied on the TCPA, the internal fibers tends to untwist in the same manner as it is done for STPAs but the new coiled and torsional constrains configuration traduces this tendency to untwist in linear actuation. TCPAs can contract about 500% more than the precursor monofilament does under the same increment of temperature [1]. Twisted polymer actuators (TPAs) is used as a general term that refers to both: TCPAs and STPAs.

Twisted polymer actuators have potential use as artificial muscles in the bio-

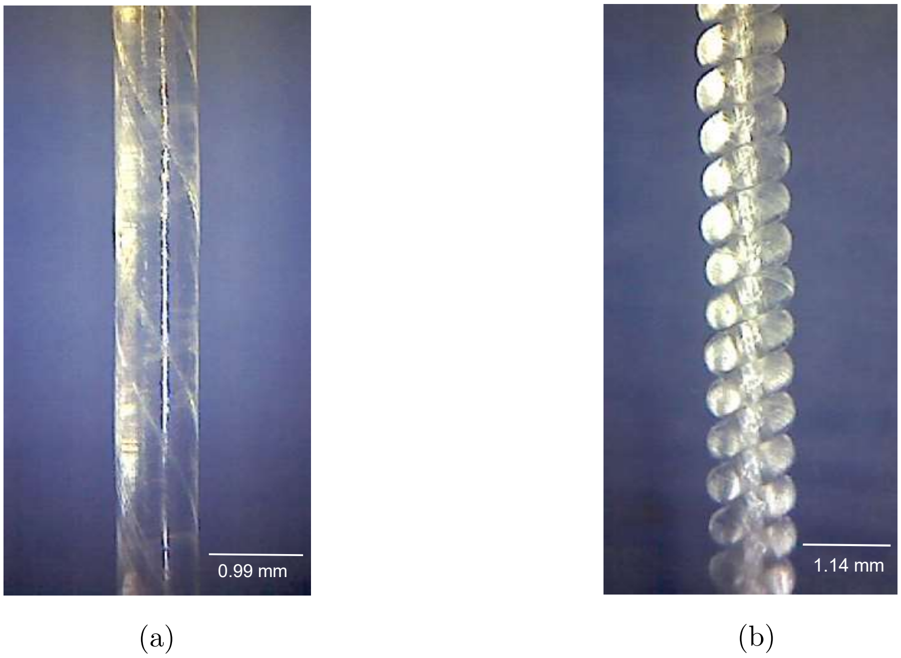

(a) (b)

Figure 1.1: (a) Torsional actuator, a.k.a. straight twisted polymer actuator (STPA); (b) linear polymer actuators, a.k.a. twisted coiled polymer actuators (TCPAs).

engineering and robotic fields since they develop maximum forces a hundred times stronger that human muscles for the same mass with contractions of 20 percent [1, 7]. TPAs have a good relationship between the work they can deliver and their size, which is a critical factor for artificial muscles applications. Furthermore, they can be used as smart textiles by stringing various TPAs together [1], or smart prosthetics [11] with the goal of assisting individuals with disabilities in basic motions.

The benefits of TPAs as actuators have driven researchers to investigate their thermo-mechanical actuation mechanisms as well as model their actuation behavior [3, 2, 12, 13, 14]. Some actuation models for TPAs use the thermo-mechanical properties of a precursor drawn monofilament so that initial twist can be designed. In this thesis, I characterize the primary mechanical properties of the precursor monofilament and study how these properties behave as a function of time and temperature with the aim to used these parameters as inputs in actuation models.

## 1.2 Aim of research

This thesis aims to characterize the mechanical and thermal properties of the precursor monofilament used to make TPAs. The thermo-mechanical properties of the precursor monofilament can be used as principal inputs parameters in actuation models, such as Shafer et al. [3] and Aziz et al. models [2] (torsional actuation) as well as Yang et al. model [14] (linear actuation). In the characterization of the properties, two different models will be considered: linear elastic model (time independent) and linear viscoelastic model (time dependent). After materials properties are presented, free torsional experimental actuation as well as actuation under load are presented for future comparison between actuation models and experimental results.

## 1.3 Thesis outline

Chapter 2 is a literature review that begins with a comparison of TPAs to existing actuation technology. Next, chapter 2 presents background on TPAs, including how TPAs actuate, are used, and current models for torsional and linear actuation. Finally, it is introduced a linear elastic and a viscoelastic material models for nylon using properties that will be identified in this work.

In the chapter 3, I present a generic protocol for the preparation of samples before testing. Next, I show the experimental set-ups, the methods, and the results used for the properties acquisition, such as axial modulus, $E_1$, shear modulus, $G_{12}$, radial modulus, $E_2$, Poisson's ratio, $\nu_{12}$, axial thermal contraction, $\varepsilon_{11}^T$, and radial thermal expansion, $\varepsilon_{22}^T$ data. The material properties are collected as a function of temperature under the assumption of linear elasticity (time independent) and as a function of time to study its viscoelastic effects (time dependent).

Chapter 4 presents experimental actuation data as well as experimental methods for different test conditions: free torsional actuation and torsional actuation under an isotonic torsional load. For the isotopic load test, actuation is performed for two different configurations: single monofilament and a parallel triple strand arrangement.

## Chapter 2

# Literature Review

In this literature review, I begin with a comparison of TPAs to existing actuation technologies. Next, I present background on TPAs, including how TPAs actuate, are used, and are modeled. Finally, I introduce material models for characterizing the precursor monofilament of nylon using properties that will be identified in this work.

## 2.1 State of the art in active material based actuation

Smart materials can be classified according to the type of actuation they deliver. The two primary groups, linear and torsional actuators, will be discussed in this section.

### 2.1.1 Linear actuation technology

The following technologies have been used for linear actuation and as such can be compared to human muscles: Lead Zirconate Titanate Piezoelectric Ceramics (PZTs), Electroactive Polymers (EAPs), Shape Memory Alloys (SMAs), Magnetic

Shape Memory Alloys (MSMAs), Shape Memory Polymers (SMPs), McKibben actuators, a.k.a. Pneumatic Artificial Muscles (PAMs), Carbon Nanotubes (CNTs), and Twisted Coiled Polymer Actuators (TCPAs), which is a type of TPA.

Tables 2.1 and 2.2 provide information on the main features, as well as advantages and disadvantages of some smart materials used as linear actuator technology. In Table 2.1 specific gravity is calculated as a ratio of density of a particular substance with that of water. Furthermore, properties and characteristics of human muscles [15] have been included to Tables 2.1 and 2.2 for comparison. Additional details on the linear actuator technologies are given below:

- Piezoelectric materials fall into the category of ferroelectric (spontaneous electric polarization that can reverse by the application of an external electric field). The most popular piezoelectrics are piezoceramics, such as lead zirconate titanate (PZT). PZTs have an electric-mechanical coupling that allows the generation of an electric charge when it deforms. This material is primarily used in sensors such as strain gauges, pressure transducers, and accelerometers [16]. However, PZTs can also be used as linear actuators, able to achieve high actuation force but a very low linear displacement. Brittleness, susceptible to cracking, and low displacement are some disadvantages, but low displacement can be solved by staking numerous of PZT sheets. [16, 17].

- Electroactive polymers (EAPs) are classified as high strain actuators due to their low elastic modulus (1 to 10 MPa) [10]. This smart material is normally presented in a sandwich configuration with a soft insulating elastomer membrane between two compliant electrodes. The actuation is driven under an

Table 2.1: Properties for linear actuation technologies.

| **Ref.** | **Type of Axial Actuator** | **Activation Mechanism** | **Specific gravity** | **Free displacement (%)** | **Actuation Stress. (MPa)** | **Magnitude of activation.** |
|---|---|---|---|---|---|---|
| [16, 17] | PZTs (Piezoelectric ceramic) | Electricity | 7.7 | 0.1 | 100 | 2 V/$\mu$m |
| [10] | EAPs Ion-based (Acrylic) (Dielectric Elastomer) | Electricity | 3.4 | <200 | 8 | $\sim$ (100 - 200) V/$\mu$m |
| [10] | EAPs Silicone (Dielectric Elastomer) | Electricity | 3.4 | $\sim$40 | 3 | $\sim$ 140 V/$\mu$m |
| [18] | SMAs (Shape Memory Alloy) | Temperature | 6.5 | 8 | >200 | $\sim$ (60 - 90)°C |
| [16, 17] | MSMAs (Magnetic Shape Memory Alloy) | Magnetism | 9 | $\sim$ 6 | <4 | $\sim$ (0.5 - 0.8) T |
| [9] | SMP (Shape Memory Polymers) | Temperature | 1.12 | $\sim$ 100 | 4 | $\sim$ (0 - 90)°C |
| [19] | PAMs (Pneumatic Artificial Muscles) | Pneumatic | 0.315 | $\sim$ 85 | $\sim$0.21 | $\sim$ 90 KPa |
| [8] | CNT (Carbon Nanotubes) | Electricity | $\sim$2.1 | $\sim$ 1 | $\sim$ 1 | $\sim$ (0 - 12) V/$\mu$m |
| [20, 21, 1] | TCPAs | Temperature | 1.12 | $\sim$ 40 | $\sim$ (0 - 75) | $\sim$ (0 - 90)°)C |
| [15] | Natural Muscle (Human Skeletal) | Chemical | 1 | >40 | 0.35 | N/A |

Table 2.2: Advantages and disadvantages for linear actuation technologies.

| **Ref.** | **Type of Axial Actuator** | **Advantages** | **Disadvantages** |
|---|---|---|---|
| [16, 17] | PZTs (Piezoelectric ceramic) | -Excellent sensory skills. | -Limited stroke under loads. (Stack configuration is a solution). |
| [10] | EAPs Ion-based actuation (Acrylic) (Dielectric elastomer) and Silicone (Dielectric elastomer) | -Easy electric activation. | -Complex manufacturing.<br>-Low free stroke. (It requires long length to deploy feasible axial actuation). |
| [18] | SMAs (Shape Memory Alloy) | -High specific strength.<br>-High stress in actuation and developed stroke. | -Tenacious material difficult to manufacture.<br>-Uneconomical.<br>-Difficult control under ambient temperature changes. |
| [16, 17] | MSMAs (Magnetic Shape Memory Alloy) | -Exclusive magnetic field of actuation. | -Very small strokes.<br>-Extremely expensive material. |
| [9] | SMP (Shape Memory Polymers) | -Large deformation<br>-Low energy consumption for shape programming.<br>-Facil manufacturability. | -High time response.<br>-Low stiffness for un-reinforced SMPs.<br>-Viscoelastic behavior. |
| [19] | PAMs (Pneumatic Artificial Muscles) | -High free displacement and blocked force | -Pressure source is required |
| [8] | CNT (Carbon Nanotubes) | - Great specific energy.<br>-Top mechanical properties. | -Very expensive material due to its extraction.<br>-This material is not practical in axial actuation. |
| [20, 21, 1] | TCPAs | -Economic.<br>-High specific strength.<br>-High stress for great strokes. | -Low thermal efficiency.<br>- Viscoelastic behavior.<br>-Difficult control under ambient temperature changes. |
| [22] | Natural Muscle (Human Skeletal) | -Compliant<br>-High specific power and work capacity<br>-Good energy dissipation | -High complexity<br>-Difficult implementation in engineering systems |

electric field generated by the applied voltage between the electrodes. When this occurs, the elactomeric membrane deforms and a high bending angle appears that can be used as linear actuation. While different types of EAPs can be considered, the characteristics of Acrylic and Silicon Dielectric Elastomers are in Tables 2.1 and 2.2 because are found to deploy the best performances in terms of linear actuation [10].

- The most common shape memory alloy (SMA) is Nitanol. SMAs have the ability to recover their shape after being deformed. Actuation can be achieved by the phase transformation of the material, when the SMA is heated from its matertensitic temperature to its austenitic temperature. The material is able to achieve high actuation force and displacement (a.k.a stroke), along with a high work capacity [23]. Although this material is appropriate for many applications, when uncontrolled external temperature gradients are present (e.g. ambient temperature changes), the actuation is affected and control of the actuation is difficult [24].
- Magnetic shape memory alloys (MSMA) are another smart materials based on the shape memory effect. Also called "Ferromagnetic Shape Memory Alloys" (FSMAs), they produce force and deformation in response to a magnetic field. MSMAs are typically single crystals of Nickel, Manganese and Gallium. When a magnetic field is applied, the magnetocrystalline anisotropy of MSMAs forces the random orientation of the dipoles to align, leading to a deformation. This is due to the rearrangement of the martensitic twin variants in the martensitic phase [16, 17]. Even though MSMAs have the ability to produce linear

actuation, the forces they are capable of lifting are quite small.

- Similarly to the shape memory effect materials, shape memory polymers (SMPs) retain a specific shape in its "memory" and after deforming, it is capable to recover the memorized shape by thermal stimulus [9]; however, this recovery can also be conducted by others means, including electric and magnetic fields, based on how they have been fabricated [25], making SMPs quite promising for actuation applications.

- McKibben artificial muscles, a.k.a. Pneumatic Artificial Muscles (PAMs), are pneumatic actuators patented by J. L. Mckibben [26, 27], which does not fall into the group of active materials but is included in this literature review because their biomimetic form and similarities to TPAs. Mckibben artificial muscles develop actuation by the change in shape and volume of an inflatable bladder surrounded by a double-helix-braided sheath. By applying pressure inside the elastomeric bladder, it contracts in length and expand radially. These actuators provide high free linear stroke due to the elasticity of the inflatable bladder, but it can also develop high block forces based on its configuration [19]. This technology has been mainly found in the robotic field, such as manipulation and joint control of robotic arms [27].

- Carbon nanotubes (CNTs) have been used in linear actuators as well [8]. Tissaphern et al. [8] reported on actuation in high tensile strength twisted single-ply yarns of carbon nanotubes submerged in an electrolyte. The tested samples of 12 mm length with a 18 $\mu$m diameter were loaded to 11 MPa and then relaxed for 30 minutes. The twisted single-ply yarn was immersed in an electrolyte of tetrabutylammonium hexafluorophosphate (TBAP) and acetonitrile (AN) showing changes in strain when a voltage input was applied. Strains of up to 0.5% are obtained in response to applied potentials of 2.5 V. One important disadvantage of this smart material is its expense due to its fabrication process.

- Finally, twisted coiled polymer actuators are thermally driven linear actuators shown to be one hundred times stronger per unit mass than human muscles [20, 21, 1, 28]. These actuators are created when the monofilament no longer can twist and coils occur, forming their characteristic spring shape, which is comprised of twisted elements. The actuation is claimed to be driven by the anisotropic thermal expansion in the radial and axial directions [1]. TPAs are made of drawn polymer monofilaments like fishing line, which makes them very inexpensive, unlike other linear actuators with similar characteristics. This low cost will allow fast and extensive implementation of this technology in the actuation field. Furthermore, TCPAs are found to have a high work capacity and quick actuation response if compare with similar actuators [20]. Potential applications in bioengineering have been proposed due to their bio-compatibility [1].

### 2.1.2 Torsional actuation technology

Many different active materials have been studied to create torsional actuation. The following technologies take a critical role in this field: Shape Memory Alloys (SMAs), Shape Memory Polymers (SMPs), Electroactive Polymers (EAPs), Pneumatic Arti-

Table 2.3: Properties for torsional actuation technologies.

| **Ref.** | **Type of Torsional Actuator** | **Activation Mechanism** | **Specific gravity** | **Free torsion. (°/mm)** | **Torque normalized by cross sectional (N/mm)** | **Magnitude of activation** |
|---|---|---|---|---|---|---|
| [5] | SMA | Temperature | 6.5 | 0.18 | ∼ (100 - 200) | ∼ (0 - 100)°C |
| [29] | SMP Shape Memory Polymers | Temperature | 1.12 | ∼1.8 | ∼1 | ∼ (0 - 62)°C |
| [30] | EAPs Ion-based actuation | Electricity | 1.12 | 0.01 | Unknown | ∼ (100 - 200) V/$\mu$m |
| [31] | PAMs (Antagonistic Torsion Shape Actuators) | Pneumatic (Pressure) | 0.315 | 0.287 | ∼ (0 - 1.43) | ∼ (50 - 90) kPa |
| [31] | PAMs (Peano Actuators) | Pneumatic (Pressure) | 0.315 | 0.315 | ∼ (0 - 0.713) | ∼ (50 - 90) kPa |
| [6, 32, 33] | CNT | Temperature | 1.6 | ∼ (15 - 80) | ∼ (0.5 - 1.8) | ∼ (0 - 90)°C |
| [3, 34, 1] | STPA | Temperature | 1.12 | ∼ 12.7 | ∼ (0 - 119) | ∼ (0 - 90)°C |

ficial Muscles (PAMs) and Hydraulic Artificial Muscles (HAMs), Carbon Nanotubes (CNTs), and finally the one studied in this research Straight Twisted Polymer Actuators (STPAs).

Tables 2.3 provides a summary of properties where specific gravity is calculated as a ratio of a density of particular substance with that of water. Table 2.4 shows a set of advantages and disadvantages of these technologies, and each are described in more detail below:

Table 2.4: Advantages and disadvantages for torsional actuation technologies.

| **Ref.** | **Type of Torsional Actuator** | **Advantages** | **Disadvantages** |
|---|---|---|---|
| [5] | SMA | -High torque for small actuator.<br>-High specific strength.<br>-Efficient. | -Tenacious material is difficult to manufacture<br>-Uneconomical. |
| [29] | SMP Shape Memory Polymers | -Large deformation.<br>-Low energy consumption for shape programming.<br>-Excellent manufacturability along with a low energy consumption | -High time response.<br>-Low stiffness for un-reinforced SMPs. |
| [30] | EAPs Ion-based actuation | -Easy activation.<br>-No high voltage required. | -Complex manufacturing.<br>-Low free torsion.<br>(It requires a long sample to deploy feasible torsion). |
| [31] | PAMs (Antagonistic Torsion Shape and Peano Actuators) | -Useful for big size applications | -The torsional actuation is not totally insolated of linear actuation.<br>-A source of pressure is required. |
| [6, 32, 33] | CNT | -Highest level of free torsion.<br>-Low specific gravity.<br>-High performance in mechanical properties. | -Low level of normalized torque.<br>-Uneconomical. |
| [3, 34, 1] | STPA | -Economic material<br>-High specific strength.<br>-High torque for a reasonable amount of free torsion. | -Low thermal activation efficiency. |

- The company Northrop Grumman with the support of NASA, has done research on SMA NiTi twisted tubes [5]. During the fabrication process, a tube was manufactured with an initial twist angle when the material was at its martensitic phase (initial state). Similarly to linear actuation, when the material phase changes from martensite to austenite by reaching the transformation temperature, the tube untwists based on the prescribed configuration, attempting to reach a state where the tube has no twist at its austenitic phase. This experiment was conducted under a torsional load. NiTi twisted tubes can deploy high torque actuation but low torsional displacement.

- Similar to shape memory alloys, shape memory polymers can achieve torsional actuation when the transition temperature is reached. Actuation can also be triggered by an electrical or magnetic field [25]. This material is featured with the capacity of retaining two or even three shapes, under specific configurations. SMPs have potential in applications for active medical devices due to their biofunctional or biodegradable characteristics [29]. Even though SMPs is mainly used in linear actuation, they also present good torsional displacement and torque results.

- Electroactive polymers actuate torsionally through the transportation of ions in and out of the polymer matrix during reduction-oxidation (redox) reactions, inducing volumetric changes, namely swelling or dswelling. Ion migration is the primary actuation mechanism for conjugation polymers [30]. EAPs have been studied as torsional actuators, but the actuation response has been found limited to torsional free displacement.

- Pneumatic artificial muscles are balloons of impermeable textile, designed with a spiral configuration to actuate as torsional actuators. When they inflate with air, they untwist. This type of technology is widely used in the robotics field [31]. Sanan et al. present average actuation results for PAMs in torque and torsional free displacement; however these results can vary based on its configuration. In Tables 2.3 and 2.4 actuation properties are presented for two different PAMs configurations, antagonistic torsion shape and Peano actuators, where their advantages and disadvantages are presented together since they are alike. The antagonist torsion shape configuration are the combination of two oppositely oriented helix (linear PAMs actuators) of an inextensible fabric that are joined along the central axis. When they are inflated, the length of the actuator remains constant, leading to torsional actuation. Peano actuators are cylinders that utilize space filling curves to create surface actuators connected in parallel around the cylinder. The torsional actuation is produced by the helical arrangement when the individual surface actuators are inflated. Note that HAMs could work in a similar way as torsional actuators, but have not been widely used as such.

- Research has been conducted on how CNTs can be used for torsional actuation [6, 32, 33]. This smart material delivers torsional actuation due to volume changes of infiltrated phase-change material (PCM) inserted in the pores of the twisted carbon nanotube yarn. Changes in temperature generate the migration of ions in and out, producing variations in the PCM, causing untwist of the CNT torsional actuator. This technology applies significant torsional displacement, thus CNT technology has been used for torsional actuators of micro-motors [6].

- Straight twisted polymer actuators are twisted monofilaments of drawn polymers where the precursor monofilament is twisted about its central axis, but still remains straight. They develop torsional actuation due to asymmetric thermal response, as TCPAs do. However, a different type of actuation is achieved based on their different configuration. Under only thermal loading this smart material will untwist and produce free torsional displacement [3], and under mechanical and thermal loading will produce torque as well as torsional displacement [34, 1]. This smart material allows for the creation of very small torsional actuators, which is difficult with the conventional technologies. As previously mentioned, the low cost of this material makes it a strong competitor in the field of actuation, and its bio-compatibility gives it the possibility to be implemented in the bioengineering field [1].

## 2.2 Twisted polymer actuators

It was recently shown that drawn polymer monofilaments, such as nylon fishing line or sewing thread, have the ability to supply linear actuation when they are configured as a coil [20]. Furthermore, this same material can be implemented as a torsional actuator when it has a twisted configuration without reaching the coiling shape [3, 34]. In this work, nylon drawn monofilaments of fishing line are used to create TPAs. In this section, I introduce the main characteristics of linear and torsional polymer actuators.

### Torsional actuation

A precursor monofilament is considered to be a straight drawn polymer monofilament (monofilament of fishing line), while a twisted monofilament is one where the precursor is twisted about its central axis, but still remains straight with the polymer chains following a helically orientation about the central axis as shown in Figure 2.1(c). This configuration was named "straight-twisted polymer actuator" (STPA) [34]. After twisting the monofilament under a tensile load, the STPA is annealed at 120°C for 20 minutes. This temperature is found to be moderately under the glass transition temperature of the material, which is 150°C [35]. The annealing process relieves the internal stresses and maintaining the twisted shape. In other words, the internal fibers have a new orientation defined by the given pitch angle, $\alpha$, which is the angle defined by the new internal fiber orientation with respect the horizontal (Figure 2.1(a)). This angle $\alpha$ depends on the radial position within the twisted monofilament (Figure 2.1(d)). The activation temperatures are defined in a range from room temperature (22°C) and 100°C. The maximum activation temperature is 20°C lower that the annealing temperature to avoid new rearrangement in the microstructure of the actuator.

After the STPA is created, Figure 2.1(b) shows the torsional actuation, as well as radial expansion and axial contraction under a thermal load.

As the fibers are heated they contract longitudinally in the new direction driven by the pitch angle and expand in the radial direction. Thus, the anisotropic ther-

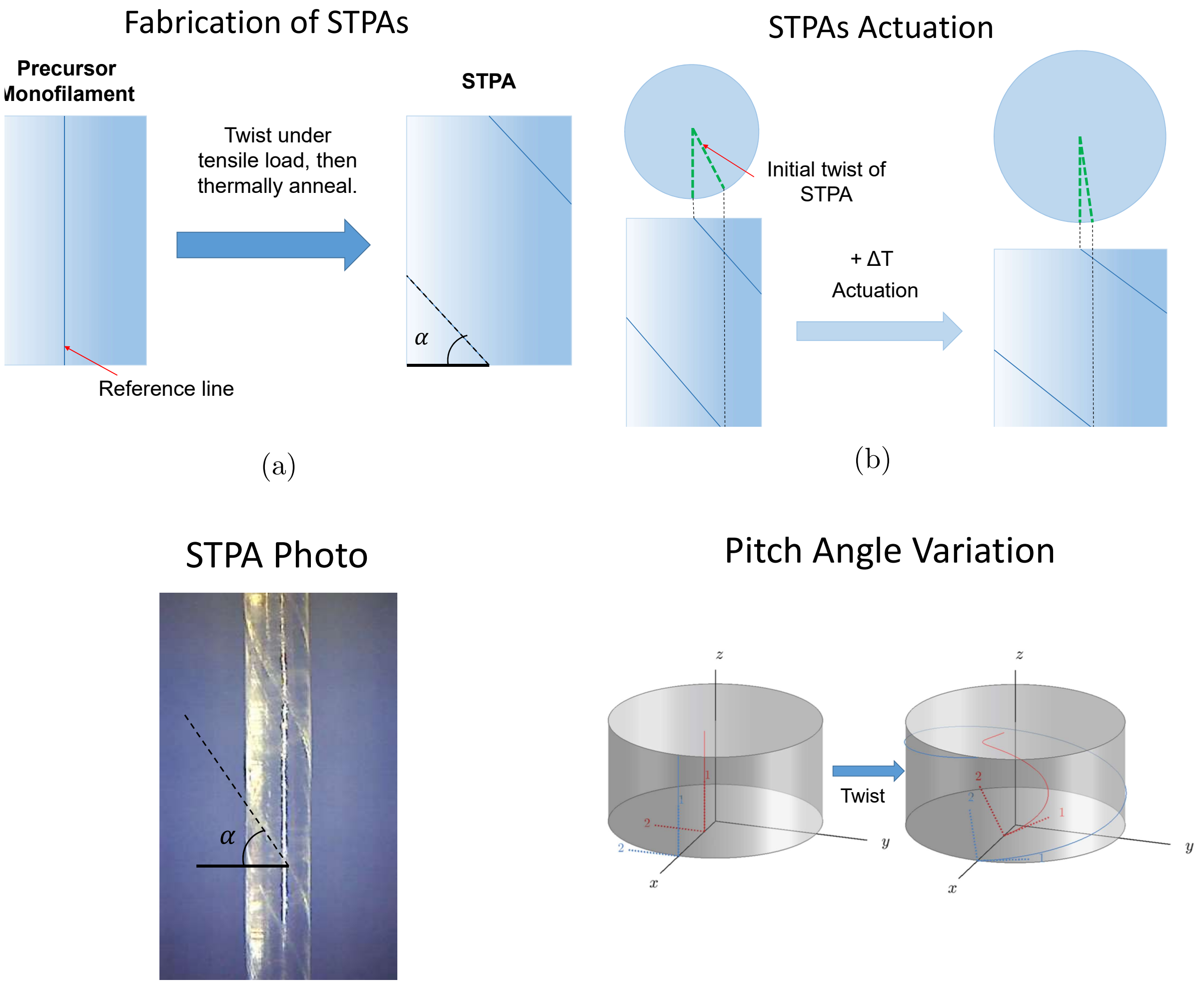

Fabrication of STPAs

STPAs Actuation

STPA Photo

Pitch Angle Variation

(a)

(b)

(c)

(d)

Figure 2.1: (a) Fabrication of a STPA with final twisted configuration after annealing; (b) initial and final state during actuation of a STPA; (c) a real STPA with indicated outer pitch angle of $\sim 60°$; (d) iso-view showing radially varying polymer chain pitch for TPAs.

mal expansion of the precursor monofilament is used in STPAs to create torsional actuation.

### Linear actuation

Twisted polymer actuators have primarily been used as linear actuators. The axial actuation is thought to be developed by the anisotropic thermal expansion in the radial and axial directions of the precursor monofilament [1]. Figure 2.2(a) displays the configuration for a linear actuator. This linear actuator is created when the monofilament torsionally buckles during twisting, such that coiling also occurs; thus, it is called a twisted coiled polymer actuator (TCPA).

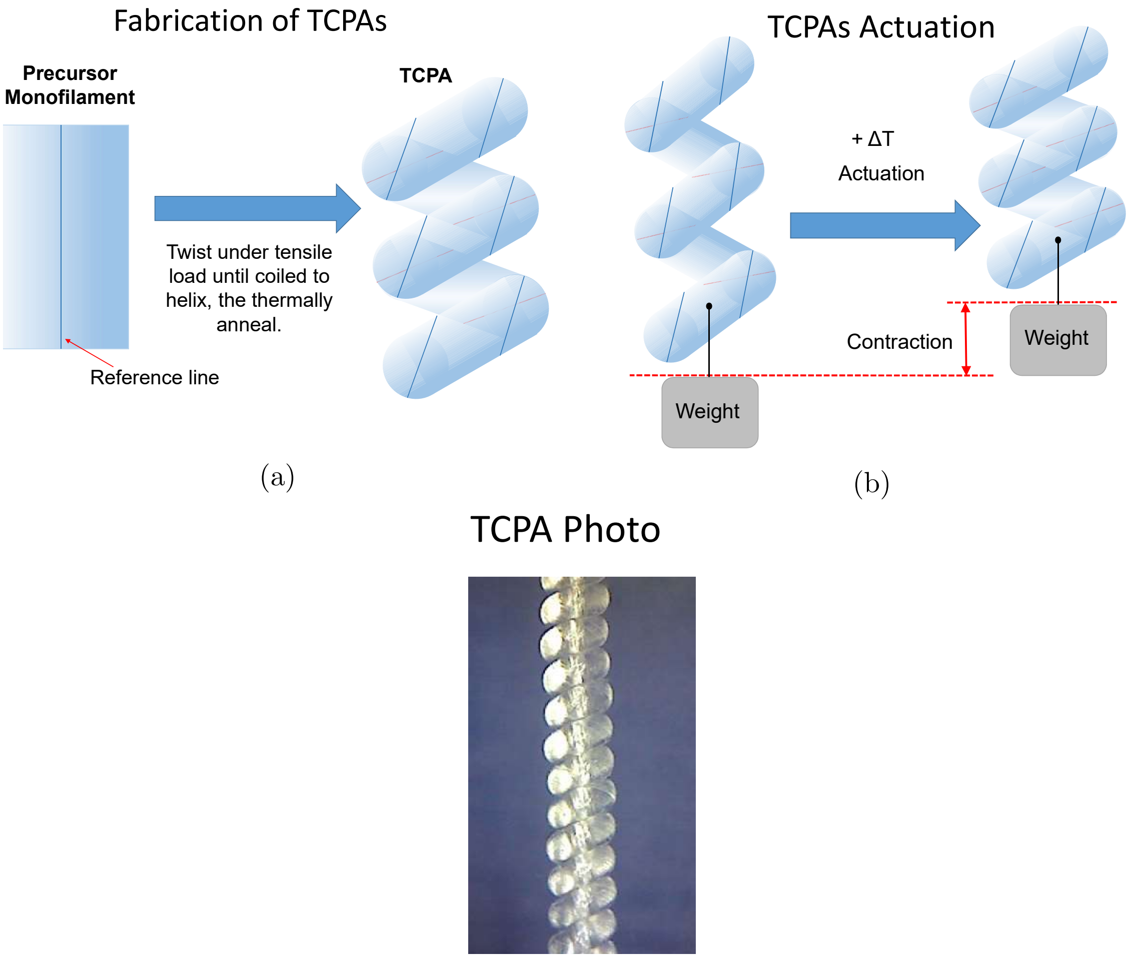

(a) (b)

(c)

Figure 2.2: (a) Fabrication of a TCPA with final coiled configuration after annealing; (b) initial and final state during actuation of a TCPA under mechanical load; (c) a real TCPA.

During actuation the TCPAs develop contraction by the same actuation mechanism as STPAs do, where the monofilament tends to untwist. In order to produce linear actuation, the sample needs to be constrained in torsion at the two ends of the actuator. Additionally, the sample can be annealed. If comparing the TCPA's contractions with the contraction of the precursor monofilament, it can be observed that TCPAs can contract about 500% more [1] under free mechanical load. Even though they contract based on the same driving forces, the TCPA's configuration leads to higher actuation displacements.

A common scenario for these linear actuators occurs when a mechanical load is applied at one end of the TCPA and as mentioned, both ends are constrained in torsion. This load stretches the coil just like a spring under tension. When the temperature is raised, the TCPA untwists and contracts, developing linear actuation (Figure 2.2(b)). An single element of a TCPA is considered to behave as a STPA, where it can be seen that linear actuation in TCPAs are produced by the untwist of the monofilament under the spring-shape configuration. Figure 2.2(c) shows a photo of a real TCPA made of fishing line of 0.28 mm in diameter and a 0.76 mm of coil diameter.

## 2.3 Microstructure of drawn polymer monofilament

The actuation of both STPAs and TCPAs is thought to be due to the asymmetric thermal expansion of the precursor monofilament, which is believed to be due to the microstructure of drawn polymers. Drawn monofilaments of nylon are semicrystaline polyamides. Their microstructure of semicrystaline polymers normally consists of crystalline regions (perfect alignment of polymer chains) and amorphous regions, which can be described as "bowl of spaghetti" [36], (high disorder of polymer chains). Research has been conducted by D.C Prevorsek et al. [36, 4], Choy et al. [37], Elad and Schultz [38], and Bukosek and Prevorsek [39] on the microstructure of drawn

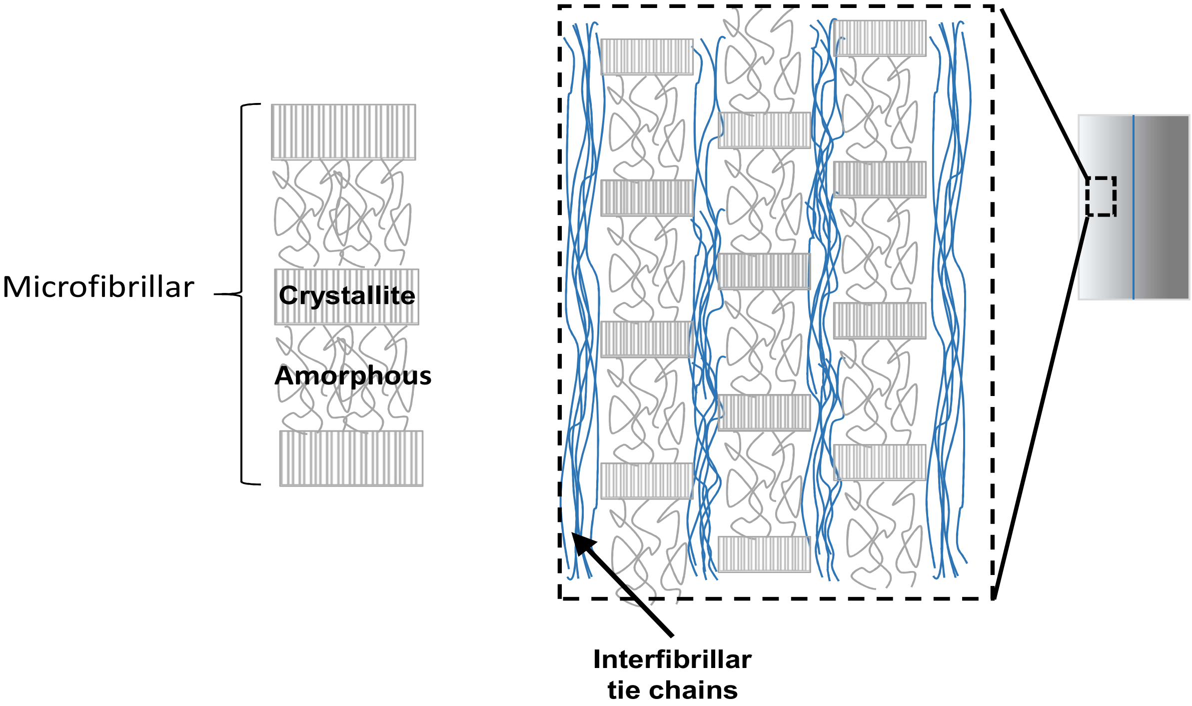

Figure 2.3: Prevorsek at el. model for the microstructure of nylon 6,6 [36].

monofilaments of nylon, showing that nylon is composed of three main domains of different properties: crystalline regions, amorphous regions, and interfibrillar tie chain molecules. Figure 2.3 shows crystallite and amorphous regions are connected to each other in a series configuration, forming what are known as microfibrillar regions. The interfibrillar tie chain molecules are aligned with the draw direction and much longer than the microfibrillar regions. The interfibrillar tie chains are located between the microfibrillar regions and their role is to bridge/tie these regions. The anisotropic properties of the precursor monofilament is thought to be due to the asymmetry of this microstructure.

As the draw ratio increases, an increase in strength and modulus occurs because a higher level of order in the interfibrillar tie chains phase is achieved [36, 4]. In other words, the polymer chains inside the monofilament become more aligned with the drawn direction. Bruno et al. [40] indicate that negative thermal expansion along the polymer chains or microfibrillar regions (axial direction) is due to the tension caused by atomic vibrations in the interfibrillar molecules. Simultaneously, this effect contributes to the expansion perpendicular to the microfibrillar region.

After the polymer monofilament is twisted, and the polymer actuator is created, the internal fiber direction is now in the given orientation defined by the pitch angle. Thus, when the STPA is heated, the internal fibers will contract in its new longitudinal direction and the monofilament will untwist. As a result, it is believed that the main driving force for the actuation is the axial contraction and resulting radial expansion produced in the interfibrillar tie chains molecules.

## 2.4 Applications of TPAs

Torsional actuators are those that produce rotatory motion or torque, meaning that the actuator revolves on a circular path. Linear actuators move forward or backwards on a set linear path. In this section, I present applications for STPAs and TCPAs in torsional and linear actuation, respectively.

### Torsional actuation (STPAs)

STPAs have not been extensively used in applications; however, there is the potential for use in different engineering applications. For example, small, lightweight, and strong actuators are needed in microrobotics, where the actuators are required to be on the scale of small bodyparts like facial muscles [11, 7, 1]. STPAs could also be used as EAPs have [41] in microfluics field. In this applications, control and manipulation of fluids are required on the scale of sub-milimeters, which STPAs could supply if carefully designed. The last field to be highlighted for potential use of STPAs is the bioengineering sector, where smart prosthetics are designed to assist or substitute human muscles. Intelligent textiles can achieve similar goals by implementing STPA threads in smart prosthetic applications [1].

### Linear actuation (TCPAs)

A larger scope of applications have been investigated for linear actuators and the most popular one is artificial muscles. According to Madden et al. skeletal muscles can contract by 20 percent in length, and each square centimeter can lift about four kilograms. Studies have reported that TCPAs can displace the same distance and furthermore, they can lift a hundred times more weight [20, 21, 1, 28]. Therefore, TCPAs can substitute human muscles and provide new possibilities to technologies in development in bioengineering and robotic fields [1, 7].

TCPAs can be used as thread that allows the formation of intelligent textiles by stringing them together, [1] as seen in Figure 2.4, or smart prosthetics [11]. TCPAs could also be used in the field of robotics in place of pneumatic and hydraulic actuators, since size is a significant factor. TCPAs are shown to performance robot joints motions by combining TCPAs, similarly as human muscles [7, 42, 12]. One of the major advantages of using TCPAs, is their high work density, which is a critical

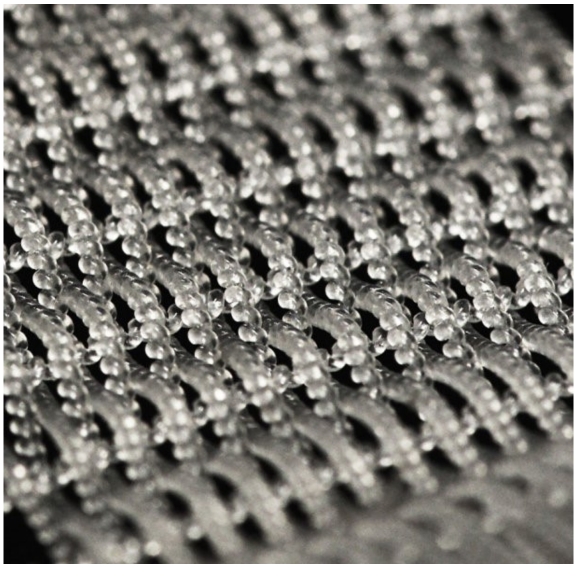

Figure 2.4: Textile made of axial polymer actuators [1].

factor for artificial muscles applications. Unfortunately, low thermal efficiency due to heat transfer losses during activation can be consider a weakness.

## 2.5 Actuation models

In order to optimize use of TPAs in applications, they must be accurately modeled mathematically. One of the aims of this thesis is to determine the material properties of precursor monofilaments needed for these models. Existing models for TPAs can be divided into two groups: torsional and linear actuation models.

### 2.5.1 Torsional actuation modeling

The torsional actuation models presented below include the Shafer et al. model [3] and the Aziz et al. model [2]. Both are kinematic models for free torsional displacement based on the thermal dimensional changes of the STPA; however, the Aziz et al. model ignores thermal axial contraction, and was only validated for temperatures between 26 and 62°C.

#### Aziz et al. Model

In the Aziz et al. model [2], torsional actuation is attributed to the radial thermal expansion. This model neglects changes in length in the axial direction of the STPA and the internal fibers for temperatures between 26 to 62°C and is therefore only valid for for these temperature range. In this model, the torsional stroke in turns per monofilament length, $\Delta T$, is predicted as

$$\Delta T = \frac{n_o}{L}\left(\frac{r_o}{r} - 1\right). \tag{2.1}$$

In Equation 2.1, $n_o$ is the initial number of twists, $r_o$ is the initial monofilament radius, $L$ is the length of the monofilament, and $r$ is the monofilament radius as a function of temperature, also shown in Figure 2.5.

Equation 2.1 can be converted in terms of change in twist, $\Delta\phi$, and the radial thermal expansion, $\varepsilon^t_{22}$, for a better comparison with other models. The prediction

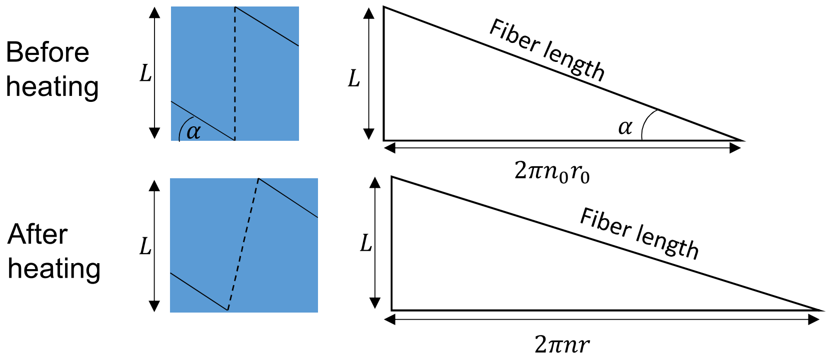

Figure 2.5: Aziz et al. model [2]. Transformation of the parameters from the initial state to the final state.

of the change in twist of the STPA in radians is given by

$$\Delta\phi = -\phi_o \frac{\varepsilon_{22}^t}{\varepsilon_{22}^t + 1}. \tag{2.2}$$

Note from Equation 2.2 that the only parameter needed in this model is the radial thermal expansion, $\varepsilon_{22}^t$.

### Shafer et al. Model

The Shafer et al. [3] model predicts the free rotation of a STPA as a function of thermal loads. The model uses the precursor drawn fiber axial thermal expansion, $\varepsilon_{11}^t$, and radial thermal expansion, $\varepsilon_{22}^t$, to predict the change in twist, $\Delta\phi$, and change in length, $\Delta L$, of the polymer monofillament under thermal loads. The following assumptions are made in this model:

- The polymer actuator is treated as a transversely isotropic bundle of polymer chains.

- It is assumed that the properties along the radial direction are isotropic.
- Because the pitch angle, $\alpha$, will vary from the center to the surface of the STPA, the free rotation will be given as a function of the radius of the STPA, even though the STPA untwist as a single unit.
- The fibers at each radii are free to expand/contract due to thermal loading and are under no stress. Note that this is not actually true as the STPA moves as a single unit and internal stresses are likely to develop.

In order to calculate change in twist and length in terms of the precursor drawn monofilament properties, a transformation of the coordinate system of the polymer chains (1 and 2 directions) to the radial, r, tangential, $\theta$, and axial, z, coordinates of the STPA has been done (See Figure 2.6). For simplification, a non-dimensional radially dependent initial twist, $x = r\phi_o/L$, has been defined, where $r$ is the radial position of a particular fiber, $\phi_o$ is the initial twist into the fiber, and $L$ the initial length of the monofilament. Figure 2.6 displays the transition of a STPA under thermal loading along with the principal and converted coordinate systems.

As a result of this coordinate transformation and simplifications, the change in length can be predicted by

$$\Delta L = \varepsilon_z^t L = \frac{\varepsilon_{22}^t x^2 + \varepsilon_{11}^t}{1 + x^2} L, \tag{2.3}$$

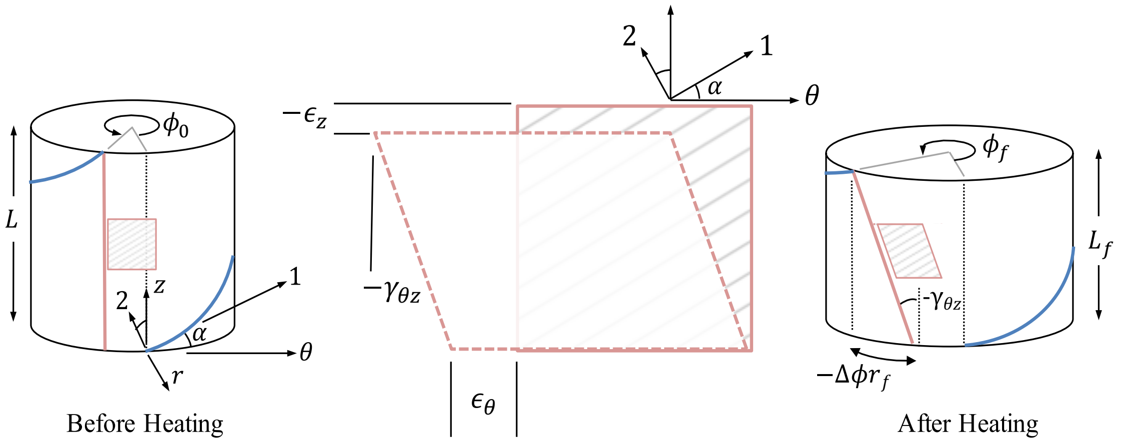

Figure 2.6: Shafer et al. model [3]. Transformation from the principal coordinates to the twisted fiber directions.

and the change in twist can be calculated using

$$\frac{\Delta\phi}{\phi_0} = \frac{(\varepsilon^t_{11} - \varepsilon^t_{22})}{1 + x^2}, \tag{2.4}$$

where the change in twist is obtained as a function of the axial thermal contraction, $\varepsilon^t_{11}$, radial thermal expansion, $\varepsilon^t_{22}$, and the parameters of the STPA.

The precursor monofilament parameters that need to be identified for Equations 2.4 and 2.3 are the axial thermal contraction, $\varepsilon^t_{11}$, and the radial thermal expansion, $\varepsilon^t_{22}$.

Comparing the Aziz et al. and Shafer model with experimental actuation results [43], Aziz et al. model under predict the actuation response for STPAs of low and high pitch angles. Part of this underprediction can be related to assuming the thermal axial contraction negligible. The Shafer et al. model present results at different radial positions [3] and average results of the actuation model [43]. Actuation predicted by this model present a tendency to underpredict the results for outer radius results, but average results aligns well with the experimental results for the high pitch angle but underpredict these results for the low pitch angle.

### 2.5.2 Linear actuation modeling

In linear actuation modeling, three models have been developed to predict the behavior of the spring shaped TCPA. Karami et al. [12] present a model based on a spring-shaped actuator under a tensile load, Sharafi et al. model [13] decomposed the actuation for temperatures below and above the coil contact temperature under no load in order to capture the effect of coils contacting each other, and finally Yang et al. [14] show a multi-scale modeling frame work using a top-down strategy under a tensile load. This section presents the linear actuation model of Yang et al. since this is the only model that uses the precursor monofilament properties to predict linear actuation. The other two [12, 13] use properties of the TCPA after fabrication. While that makes the modeling simpler, it does not allow for twist inserted during fabrication to be designed or altered. Nonetheless, Karami et al. model [12] shows good predictions during heating and cooling actuation cycles for different mechanical loads, but it does not capture the transition between heating and cooling. Shafari et al. [13] present a comparison between their model and experimental actuation results without recovery. Here, the model shows similar behavior to the experimental data but it does not follow the defined trend of actuation as a function of temperature.

**Yang et al. model (Multi-scale model)**

Yang et al. [14] have presented a multi-scale modeling framework for the thermo-mecahnical actuation of TCPAs using a top-down strategy, starting from the macro-scale and focusing down to the microstructure level of the precursor monofilaments.

The focus here is on the macroscale, where Yang et al. models the TCPA as a spring and the meso-scale, where Yang et al. models a section of TCPA as a STPA, as shown in Figure 2.7. A constant axial load, $F$, is applied to the coil to stretch the TCPA and the two ends of the actuator are constrained to prevent the TCPA from untwisting, which creates a recovered torque, $M_{rec}$. The total change in height of a TCPA, $\Delta H$, is given by

$$\Delta H(T) = f_{11}F - f_{12}M_{rec}, \tag{2.5}$$

where $f_{11}$ and $f_{12}$ are coefficients that are functions of the diameter of the precursor monofilament, $d$, the number of active coils, $n$, the final length of the monofilament, $L_c$, the pitch angle, $\alpha_c$, of the STPA section of the TCPA, and the effective Young's modulus and shear modulus of the twisted monofilament, $\overline{E}$ and $\overline{G}$, respectively [14]. These thermomechanical properties, i.e. the stiffness matrix and the coefficients of the thermal expansion of the twisted fiber, can be determined from the precursor monofilament properties using the classical lamination theory. However, that is not what Yang et al. do. Instead they go to smaller and smaller scales to approximate these properties. Then they calibrate the model to the small scale properties that are used to determine to precursor monofilament properties. Thus, they do not determine elastic mechanical and thermal properties of precursor monofilaments.

Yang et al. [14] present modeling and experimental results of the tensile actuation

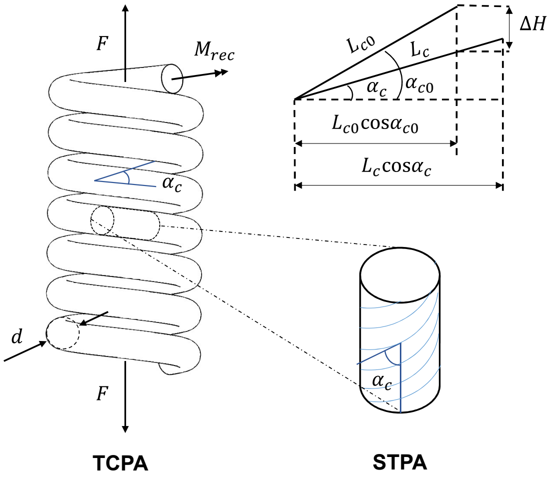

Figure 2.7: Initial and final parameters of a TCPA for the Yang et al. model.

where the model follow the actuation behavior; however, the results do not align due to the slow initial decay of the modeling results. This might be because their model does not include any viscous effects.

## 2.6 Mechanical modeling of materials

In addition to identifying parameters for models, this work also hopes to identify mechanical properties of precursor monofilaments for better understanding and future models of TPAs. In particular, future work is planed to model the actuation of TPAs under thermal and mechanical load with both closed form models and finite element simulation. Both cases will need the mechanical properties identified.

In the mechanical modeling of drawn polymers, there are two considerations to take into account that are often neglected for isotropic linear elastic materials:

anisotropic behavior and viscoelastic responses. In anisotropic materials, the properties differ depending on the direction the stresses or strains are applied. Orthotropic materials are a special case of anisotropic materials where properties differ along three mutually orthogonal axes. Drawn polymers can be further classified as transversely isotropic material, which is a special case of an orthotropic material with one axis of symmetry (in the radial direction of the precursor monofilament) [44].

The second aspect to consider is the time dependent behavior of the material when a stress is applied. Two types of behaviors are studied in this thesis: linear elastic (not time-dependent) and viscoelastic (time-dependent). The next sections will explain these two models and their differences.

### 2.6.1 Linear elastic orthotropic

In this subsection, the 3-D stress-strain relationships for a transversely isotropic material will be considered assuming linear elasticity, with the 2-3 plane is assumed to be a plane of isotropy (as shown in Figure 2.8). Thus, all properties in the radial direction are the same and different than properties in the axial direction. Assuming orthotropy, the elasticity equations are given by

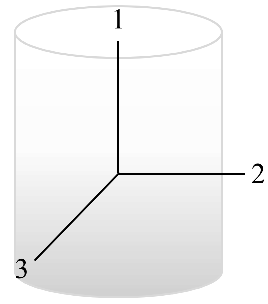

Figure 2.8: Principle directions for an orthotropic cylinder (such as a precursor monofilament).

$$\begin{Bmatrix} \varepsilon_1 \\ \varepsilon_2 \\ \varepsilon_3 \\ \gamma_{23} \\ \gamma_{13} \\ \gamma_{12} \end{Bmatrix} = \begin{bmatrix} \frac{1}{E_1} & \frac{-\nu_{21}}{E_2} & \frac{-\nu_{31}}{E_3} & 0 & 0 & 0 \\ \frac{-\nu_{12}}{E_1} & \frac{1}{E_2} & \frac{-\nu_{32}}{E_3} & 0 & 0 & 0 \\ \frac{-\nu_{13}}{E_1} & \frac{-\nu_{23}}{E_2} & \frac{1}{E_3} & 0 & 0 & 0 \\ 0 & 0 & 0 & \frac{1}{G_{23}} & 0 & 0 \\ 0 & 0 & 0 & 0 & \frac{1}{G_{13}} & 0 \\ 0 & 0 & 0 & 0 & 0 & \frac{1}{G_{12}} \end{bmatrix} \times \begin{Bmatrix} \sigma_1 \\ \sigma_2 \\ \sigma_3 \\ \tau_{23} \\ \tau_{13} \\ \tau_{12} \end{Bmatrix}. \tag{2.6}$$

Equation 2.6 can be simplified by applying the following transversely isotropic properties:

$$E_2 = E_3, \quad G_{13} = G_{12}, \quad \nu_{12} = \nu_{13}, \quad \nu_{21} = \nu_{31}, \quad \text{and} \quad \nu_{23} = \nu_{32}$$

and noting that

$$G_{23} = \frac{E_2}{2(1+\nu_{23})} = \frac{E_3}{2(1+\nu_{32})}.$$

Furthermore, we can use the symmetry of the compliance matrix to relate the following properties:

$$\left.\begin{aligned} \frac{\nu_{12}}{E_1} &= \frac{\nu_{21}}{E_2} \\ \frac{\nu_{13}}{E_1} &= \frac{\nu_{31}}{E_3} \\ \frac{\nu_{23}}{E_2} &= \frac{\nu_{32}}{E_3} \end{aligned}\right\} \text{Or, } \frac{\nu_{ij}}{E_i} = \frac{\nu_{ji}}{E_j}.$$

Thus, the final expression for the linear elastic compliance matrix for the transversely isotropic untwisted monofilament is given by

$$\begin{Bmatrix} \varepsilon_1 \\ \varepsilon_2 \\ \varepsilon_3 \\ \gamma_{23} \\ \gamma_{13} \\ \gamma_{12} \end{Bmatrix} = \begin{bmatrix} \frac{1}{E_1} & \frac{-\nu_{12}}{E_1} & \frac{-\nu_{12}}{E_1} & 0 & 0 & 0 \\ \frac{-\nu_{12}}{E_1} & \frac{1}{E_2} & \frac{-\nu_{23}}{E_2} & 0 & 0 & 0 \\ \frac{-\nu_{12}}{E_1} & \frac{-\nu_{23}}{E_2} & \frac{1}{E_2} & 0 & 0 & 0 \\ 0 & 0 & 0 & \frac{2(1+\nu_{23})}{E_2} & 0 & 0 \\ 0 & 0 & 0 & 0 & \frac{1}{G_{12}} & 0 \\ 0 & 0 & 0 & 0 & 0 & \frac{1}{G_{12}} \end{bmatrix} \times \begin{Bmatrix} \sigma_1 \\ \sigma_2 \\ \sigma_3 \\ \tau_{23} \\ \tau_{13} \\ \tau_{12} \end{Bmatrix}. \qquad (2.7)$$

Note there are five independent variables are required for an elastic model of this material:

- Axial modulus, $E_1$.
- Radial modulus, $E_2$.
- Shear modulus, $G_{12}$.

- Poisson's ratios, $\nu_{12}$ and $\nu_{23}$.

### 2.6.2 Viscoelastic orthotropic

Most polymers (including drawn monofilaments) can be classified as linear viscoelastic materials. Linear viscoelastic materials exhibit characteristics of viscous fluids and elastic solids, and therefore are time dependent. In drawn monofilaments, it is assumed that the amorphous regions are largely responsible for the viscous behavior and the crystalline regions provide a linear elastic behavior of the material (see Figure 2.10). Additionally, it has been shown that increasing the temperature boosts viscoelastic effects [44].

Viscoelastic models, such as the Maxwell model, Kelvin-Voigt model, and the Zener model, can be used to predict this viscoelastic behavior. These models are combinations of spring-dashpot elements, where the spring and dashpot capture the elastic and viscous behaviors, respectively. They are based on the Boltzmann superposition principle, where the strain response is linearly proportional to the input stress, but also a function of time.

Figure 2.9(a) shows a dashpot-spring connected in series (Maxwell model). The Kelvin-Voigt model consists of a dashpot-spring connected in parallel. Kelvin -Voigt is not used in this study because the relaxation modulus as a function of time of this model is constant, so it does not suitably capture the viscous effect of the material. Figure 2.9(b) shows the Zener model as a Maxwell model with an extra spring attached in parallel. It has been shown that the Zener model is a qualitatively suitable model that partially captures the viscoelastic effects of polymers [45]. Figure 2.10

shows the Zener model's assumed relationship between these mechanical elements and the regions in the hypothesized polymer microstructure [36]. The $k_1$ and $\mu_1$ elements represent the series combination of the crystallite and amorphous components in the mircrofibrillar region. The internal fibers, or interfibrillar tie molecules, are modeled as a spring, $k_0$, and connected in parallel. Finally, two more improved models will be used in this work: the improved parallel Zener model with two elements (two Maxwel models with an extra spring all connected in parallel) and the improved series Zener model with two elements (two Kelvin-Voigt models with an extra spring all connected in series) to better capture the viscoelastic response of the precursor monofilament (Figures 2.9(c) and 2.9(d)).

Below is a list of the relaxation modulus $C(t)$ for each of the models to be used in this work. The relaxation modulus is an expression, which is used to predict the changes of stress for a given constant strain as a function of time. The relaxation modulus is vital to study the viscous effects and find viscoelastic coefficients of the material.

- Maxwell model (Figure 2.9(a))

$$C(t) = \left(ke^{-t/\lambda}\right). \tag{2.8}$$

- Zener model (Figure 2.9(b))

$$C(t) = \left(k_0 + k_1 e^{-t/\lambda}\right). \tag{2.9}$$

- Improved parallel Zener model with two dashpot-spring elements (Figure 2.9(c))

$$C(t) = \Big(k_0 + k_1 e^{-t/\lambda_1} + k_2 e^{-t/\lambda_2}\Big). \tag{2.10}$$

- Improved series Zener model with two dashpot-spring elements (Figure 2.9(d))

$$C(t) = \Big(1/k_0 + 1/k_1 e^{-t/\lambda_1} + 1/k_2 e^{-t/\lambda_2}\Big)^{-1}. \tag{2.11}$$

In Equations 2.8, 2.9, 2.10, and 2.11 $k_i$ is the spring constant parameter and $\lambda_i$ is relaxation time defined as $\mu_i/k_i$.

By applying the equations of motion to the Zener model spring-dashpot configuration (Figure 2.10), the following linear differential equation is obtained.

$$\sigma(t) + \frac{\mu_1}{k_1}\frac{d\sigma}{dt} = k_0\varepsilon + (k_0 + k_1)\frac{\mu_1}{k_1}\frac{d\varepsilon}{dt}. \tag{2.12}$$

Equation 2.12 can be re-written by defining $\lambda = \mu_1/k_1$ and $\rho = \lambda(k_0 + k_1)/k_0$, which yields

$$\sigma(t) + \lambda\frac{d\sigma}{dt} = k_0\Big(\varepsilon + \rho\frac{d\varepsilon}{dt}\Big). \tag{2.13}$$

Equation 2.13 can be solved if the strain is held constant, as in a stress relaxation test, where a step strain of magnitude $\varepsilon_0$ is applied from time zero until $t_i$ where the subscript $i$ indicates the initial time of the recovery cycle. Afterwards, there is a recovery period, where the step strain is set back to zero, as shown in Figure 2.11. The relaxation and recovery expressions are

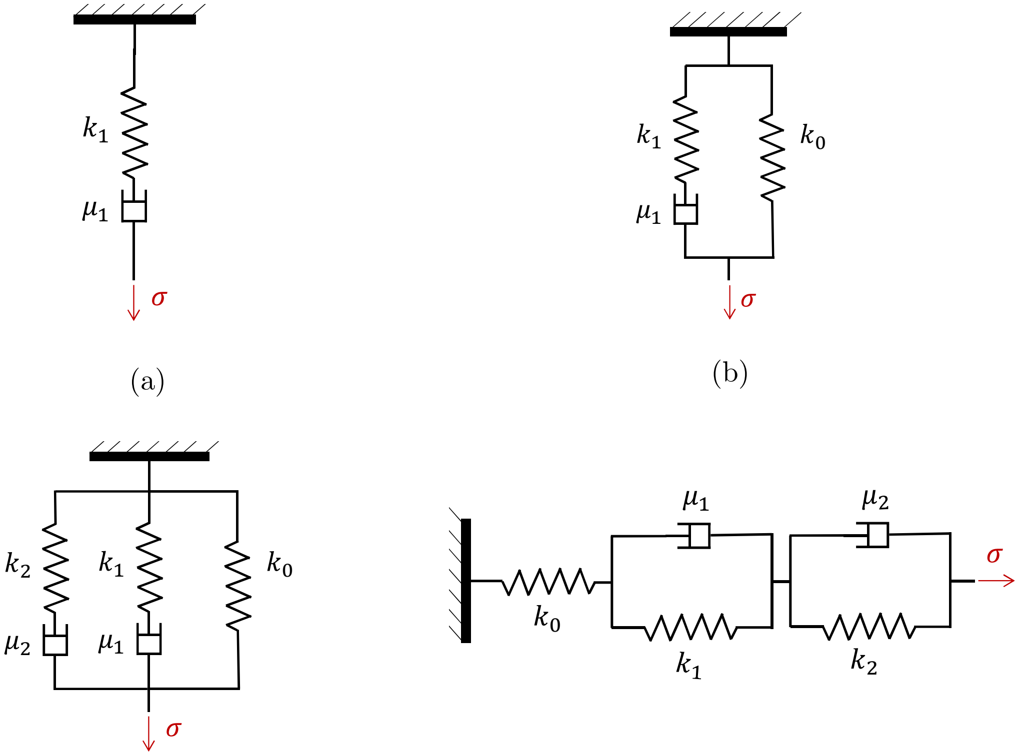

(a)

(b)

(c)

(d)

Figure 2.9: (a) Maxwell model; (b) Zener model; (c) Improved parallel Zener model with two elements; (d) Improved series Zener model with two elements

$$\sigma = \left(k_0 + k_1 e^{-t/\lambda}\right)\varepsilon_0 \qquad \text{for } (0 < t < t_i) \tag{2.14}$$

and

$$\sigma = k_1\left(e^{-t/\lambda} - e^{-(t-ti)/\lambda}\right)\varepsilon_0 \qquad \text{for } (t_i < t < t_f). \tag{2.15}$$

The viscoelastic parameters, $k_0, k_1$, and $\lambda$, can be obtained by fitting these equations to experimental data for a relaxation test. A similar curve fit to a relaxation test

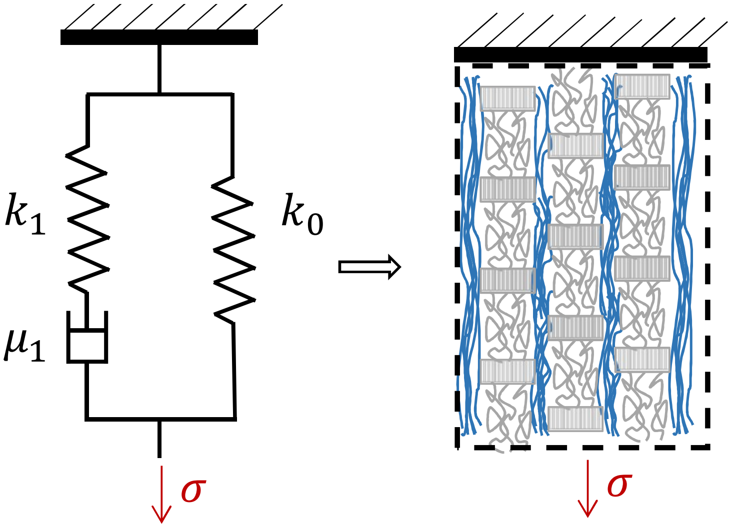

Figure 2.10: Zener model approximation to the microstructure of drawn monofilaments of nylon 6,6. [4]

can be done for the other viscoelastic models. This will be done later in this work, e.g. Section 3.4.

A Dynamic Mechanical Analysis (DMA) can also be conducted to identify the constants in a viscoelastic model. In a DMA, a continuous oscillating displacement, $\tilde{\varepsilon} = \varepsilon_0 e^{i\omega t}$, is the input. This test allows us to obtain the complex modulus, $E_c = E' + E''$, where $E'$ is the storage modulus and $E''$ is the loss modulus. The storage and loss modulus can be mathematically derived for the Zener model from Equation 2.13, and are given by

$$\sigma' = \left( k_0 + \frac{k_1 \omega^2 \lambda^2}{1 + \omega^2 \lambda^2} \right) \tilde{\varepsilon} = E' \tilde{\varepsilon}, \tag{2.16}$$

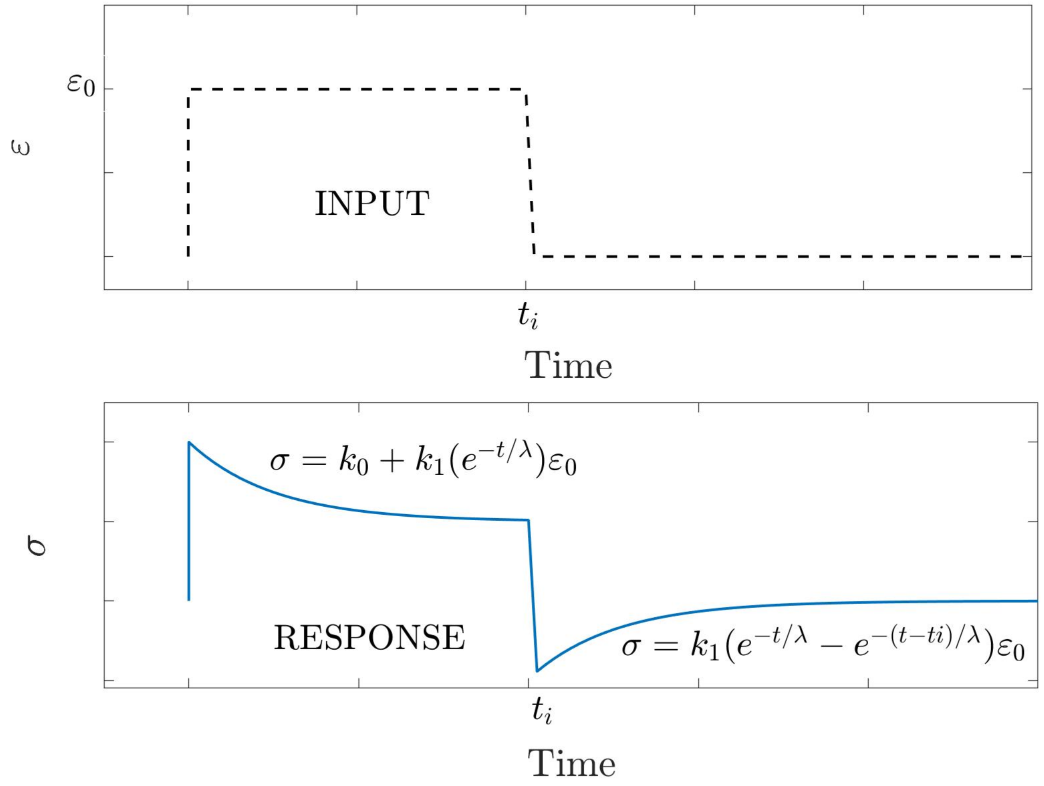

Figure 2.11: Stress relaxation and recovery with a constant step strain input

$$\sigma'' = \left(\frac{k_1 \omega \lambda}{1 + \omega^2 \lambda^2}\right)\tilde{\varepsilon} = E''\tilde{\varepsilon}, \tag{2.17}$$

where $\sigma'$ is the storage stress, and $\sigma''$ is the loss stress.

Figure 2.12 shows theoretical results for the complex of the stress, $\tilde{\sigma}$, and strain, $\tilde{\varepsilon}$, for a constant frequency. Figure 2.12(a) displays the stress-strain results as a function of time along with the phase angle, $\delta(\omega)$, which represents the time offset between strain and stress. A common result for a stress-strain test is shown in Figure 2.12(b), where hysteresis appears due to the time dependency effects. The area inside

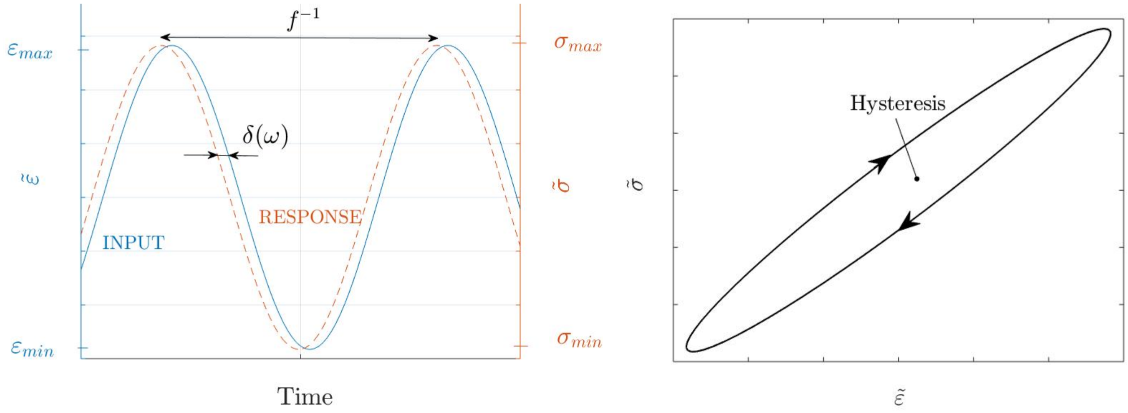

(a) (b)

Figure 2.12: (a) Dynamic test with sinusoidal strain as an input. Notice the delay in the stress response due to viscous effects; (b) hysteresis in complex stress-strain relationships typical of linear viscoelastic material.

the hysteresis loop is known as the loss energy.

Dynamic Mechanical Analysis (DMA) tests are typically conducted as a function of frequency, to understand how the storage and loss modulis change as a function of the strain rate. Similarly, DMA tests can be performed as a function of temperature to characterize the temperature dependency of the linear viscoelastic response. This thesis does not present DMA analysis, however these tests may be considered for future work.

## Chapter 3

# Characterization of the Precursor Monofilament

Reliable 3D thermal and mechanical properties have not been found for drawn monofilaments of nylon in the literature, likely due to the material's small dimension radially and the lack of need for these properties until the advent of TPAs. In this chapter, I present a generic protocol for the preparation of precursor monofilament samples before testing, describe the experimental setups and methods, used for acquiring the thermal and mechanical properties of drawn nylon, and the results for the thermal, elastic and viscoelastic properties of drawn nylon 6,6.

## 3.1 Identification of the material

The precursor drawn monofilament of nylon used in this thesis is the Berkley Trilene® Big Game™ monofilament fishing line. The 80 lbf strength line has a diameter of 0.89 mm. Identification of the material was conducted by Dr. Cindy Browder at

Northern Arizona University using Fourier transformation infrared spectroscopy to determine the composition of the monofilament. The sample was then analyzed on a Thermo Nicolet Nexus 670 FT-IR using an attenuated total reflectance attachment. After analyzing the results, nylon 6,6 was found to be the closest match to the spectral signal.

## 3.2 Fabrication and preparation

In the pursuit of collecting the properties of the drawn monofilaments, a preparation protocol of the specimen must be followed to obtain consistency in the results. With a goal of collecting the material properties as a function of temperature and time other variables that may affect these properties must be controlled. The precursor monofilament can vary as a function of other variables, such as humidity [46], and number of loading cycles, particularly in the first few cycles, known as “first cycle effect” [47, 48]. These variables can be controlled during actuation by following a consistent protocol.

### 3.2.1 Protocol of preparation of the sample

In previous works, it was found that certain environmental and manufacturing conditions of the sample, such as humidity levels and annealing can significantly affect experimental results [3, 34]. To address these variables, a standardized protocol was followed before any test was conducted in this thesis.

To straighten the samples, the precursor monofilaments were thermally treated by annealing in an oven, keeping the monofilaments clamped straight at a temperature of 120°C for 20 minutes. After thermal treatment, the samples were taken out of the oven and let them cool down to room temperature by free convection. This process guarantees alignment of the monofilaments across the axial axis and set the precursor monofilament under the same microstructural condition as the TPAs would be during actuation. Moreover, this step was required as nylon from the spools of fishing line typically has significant curvature.

After annealing, the samples were stored in desiccant, the Blue Indicating Silica Gel Granular 6-16 Mesh from Delta Adsorbents, to control the moisture level. Because of the hydrophilic behavior of polymers [46], they tend to absorb the moisture from the environment. Additionally, research has shown that certain mechanical properties, such as $E_1$, are highly dependent on moisture concentration [46]. For these reasons, all samples were kept near zero percent level of moisture.

The moisture absorption behavior of the precursor monofilament was studied in order to determine how long it takes for the moisture concentration to drop nearly to zero in the presence of desiccant and how long it takes to absorb moisture from the environment after drying. This tells us how long the sample needs to be stored in desiccant and how long the sample can be tested without significant variations in properties due to changing moisture levels. A spool of fishing line (precursor monofilament) was placed in contact with desiccant inside a sealed chamber. The spool of nylon was weighed several times over a total of nine days. Moisture concentration was not directly measured, but mass lost due to moisture in the sample was. After the weight of the material started stabilizing, the spool was taken out of the chamber and the weight was tracked over days as the sample absorbed moisture.

Figure 3.1 displays the results of this test. The weight appears to exponentially decrease when in contact with the desiccant and then exponentially increase when exposed to the environment. The change in weight due to moisture in the sample during dessication was almost 1% of the initial weight and the moisture in the sample during absorption was 0.3% of the initial weight. Since the initial moisture concentration was higher than the moisture concentration after absorption, it was concluded that the previous storage environments had a higher level of moisture concentration. This seems logical as Flagstaff, AZ is a relatively dry environment most of the year. Exponential fits for the weight of the sample as a function of time during desiccation and moisture absorption are plotted in Figure 3.1 and given by

$$W_{desiccating} = 35.46 + 0.26\ e^{\ (-t/37)} \tag{3.1}$$

$$W_{absorbing} = 35.57 - 45.39\ e^{\ (-t/19.32)}. \tag{3.2}$$

In Equations 3.1 and 3.2, the variable $t$ is the time in hours, and $W_{desiccating}$ and $W_{absorbing}$ are the masses in grams during the desiccating and absorbing processes, respectively.

During the desiccation process, the precursor monofilament did not achieve a steady state moisture level; and therefore Figure 3.1 shows an extended exponential fit for a longer period of time where total desiccation appears to be a reasonable assumption, after 150 hours (6.25 days). Thus, six to seven days is the minimum time that the samples should be stored in desiccant before testing. It must be taken into consideration that these relationships are dependent upon the humidity levels of

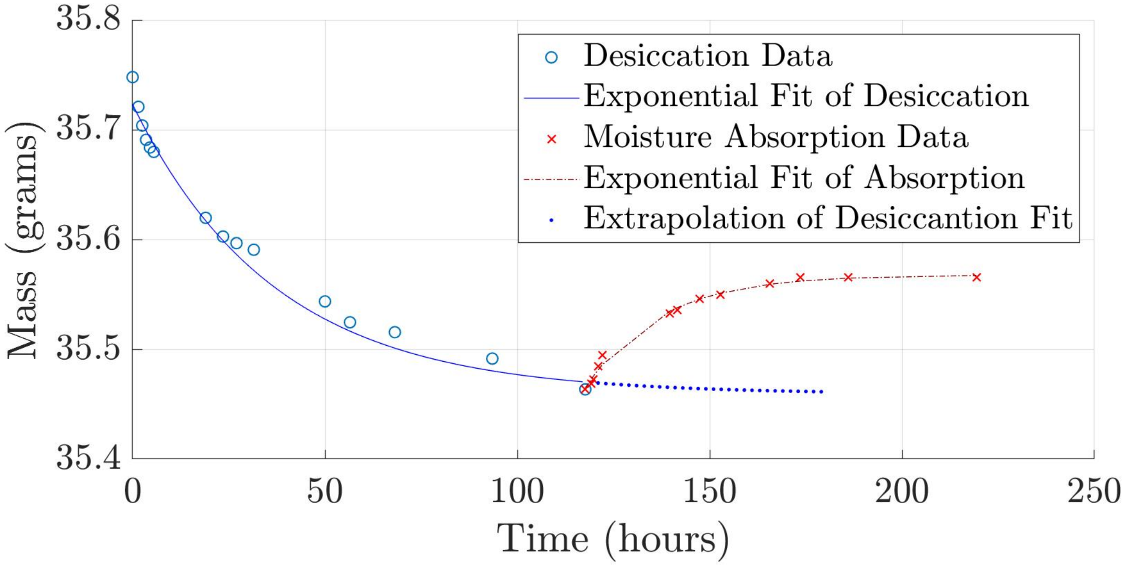

Figure 3.1: Desiccating and moisture absorbing process as a function of time along with an extended exponential fit for the dessication of the precursor monofilament.

material storage environments. Since this parameter was not measure during these tests, the samples were subsequently continuously stored in the desiccant in order to ensure a negligible level of moisture in the samples.

Finally, it is important to highlight how rapid the moisture absorption occurs once the material is pulled out of the desiccant. Approximately 11% of the final weight of the sample is recovered in the first 1.5 hours; however, this result is found to be 0.03% of the initial weight of the sample. As such, all tests were conducted within approximately 120 minutes of removal from the desiccant pack.

### 3.2.2 Thermal pre-cycling and first cycle effect

During characterization of the thermal expansion properties, a “first cycle effect” was observed, where total recovery was not reached in the first cycles but the following cycles presented full recovery. This first cycle effect (a.k.a. Mullin’s effect) is well documented by Xuebing Li et al. for cyclic stress-strain curves in nylon 6,6, where the loading and unloading are never coincident in the first few cycles under a specific load and changes in modulus occur until it yields a steady state [48]. Additionally, when a higher load is set, the first cycle effect starts again. Xuabing et al. attribute the Mullins effect to the destruction of adhesive and slippage between the internal monofilament that occur during stretching process. Even though this effect is studied under mechanical loading and not thermal loading, a similar behavior was shown by Shafer et al. [34] for STPAs, where the STPA exhibited significant permanent deformation in the first thermal cycle and minimal permanent deformation during the subsequent cycles. After four or five thermal cycles stable recovery was observed. A similar response has been found in other smart polymers, such as shape-memory polymers where this behavior is claimed to be associated with the reconfiguration of the twisted polymer chains and plastic deformation of the material [49]. Shafer et al. [34] attribute the first cycle effect to the twisted configuration and/or the pre-load applied during actuation. However, the first cycle effect has also occurred in our experimental results for most of the properties in the precursor monofilament, suggesting that the first cycle effect may be at least partially associated with the time-dependent response of the material under thermal loading.

Due to first cycle dissimilarities and thermal creep in actuation, every sample was thermally pre-cycled prior to testing by cooling and heating the sample between ambient temperature and approximately 110°C. Due to the fact that drawn monofilaments are anisotropic, the duration of the thermal precycling needed to eliminate first cycle effects varies with the direction. For most of the tests presented in this thesis a generic pre-cycling process of 30 minutes at 110°C and cooling by free convection to room temperature was conducted to remove the thermal fist cycle effect; however, for the axial modulus, shear modulus and axial thermal contraction as a function of temperature tests a different preparation procedure was followed, which is explained in their method sections.

## 3.3 Experimental setups for the precursor monofilament properties acquisition

For the acquisition of the mechanical and thermal properties of the precursor monofilament, different setups were designed. Here, I present the setups used for collecting: axial modulus, $E_1$, shear modulus, $G_{12}$, radial modulus, $E_2$, Poisson's ratio, $\nu_{12}$, axial thermal contraction, $\varepsilon_{11}^T$, and radial thermal expansion, $\varepsilon_{22}^T$ data. Note that these are all parameters in the linear elastic transversely isotropic model, except $\nu_{23}$ (see Equation 2.7). Poisson's ratio in the 2-3 direction is very difficult to measure. However, the material is isotropic in the 2-3 direction, therefore it is fair to assume that $\nu_{23}$ is equal to the Poisson's ratio for bulk nylon 6,6.

### 3.3.1 Axial modulus, $E_1$, and shear modulus, $G_{12}$, setup

The TA Instruments Hybrid Discovery Rheometer 2 (HR-2) was used to obtain the axial and shear modulus as a function of temperature and time (Figure 3.2), along with an environmental test chamber (ETC) equipped with a heating element and thermocouples. The HR-2 has the following measurement resolutions: Torque: 0.1 nN-m, Force: 0.5 mN, Rotation: 10 nrad, Axial: 0.1, $\mu$m. For other test conditions where quick changes in temperature are required, a better temperature control system was found by using a manual controlled heat gun. However, the required steady state and uniform temperature makes the ETC a suitable system in these tests.

Figure 3.2 shows the HR-2 with the attached ETC and the custom designed and fabricated torsional accessory used to clamp the sample. For these tests, a script was set to conduct a stress-strain experiment for axial modulus testing or a torque-angular displacement experiment for shear modulus testing at the desired steady state temperature while the ETC doors were closed. Finally, the temperature was measured by the ETC thermocouple. The mechanical load and gap distance (for axial modulus) or torque and angular displacement (for shear modulus) were measured by the HR-2.

### 3.3.2 Radial modulus, $E_2$, setup

Radial modulus for monofilaments are difficult to obtain due to small dimensions in the radial direction. The book, Mechanical Properties of Solid Polymers [50] presents a method where the precursor monofilament is compressed between two flat parallel plates. Under this condition, plane strain can be assumed, and thus, no axial

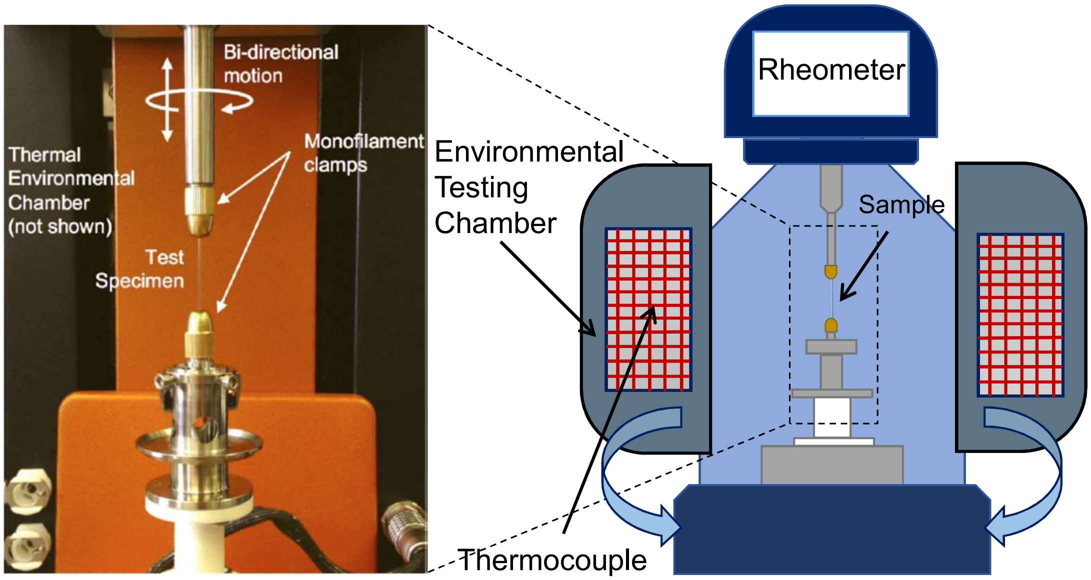

Figure 3.2: HR-2 along with the ETC system and the torsional accessory.

dimensional change occurs and only axial stress, $\sigma_{11}$, acts along the monofilament, which can be written as a function of the stresses $\sigma_{33}$ and $\sigma_{22}$ as

$$\sigma_{11} = -\frac{S_{21}}{S_{11}}(\sigma_{33} + \sigma_{22}), \tag{3.3}$$

where $S_{21}$ and $S_{11}$ are components of the compliance tensor. Figure 3.3 shows the contact zone, with dimension of 2b, which is assumed to be small compared with the precursor monofilament diameter. It is adequate to consider that the flat plates are infinite solid bodies and use Hertz's classic solution for the compression of an isotropic cylinder. In this solution, the displacement of the cylinder within the contact zone is assumed to be parabolic and the boundary conditions are satisfied along the boundary plane only. Finally, the measurable variable $b$ is given as

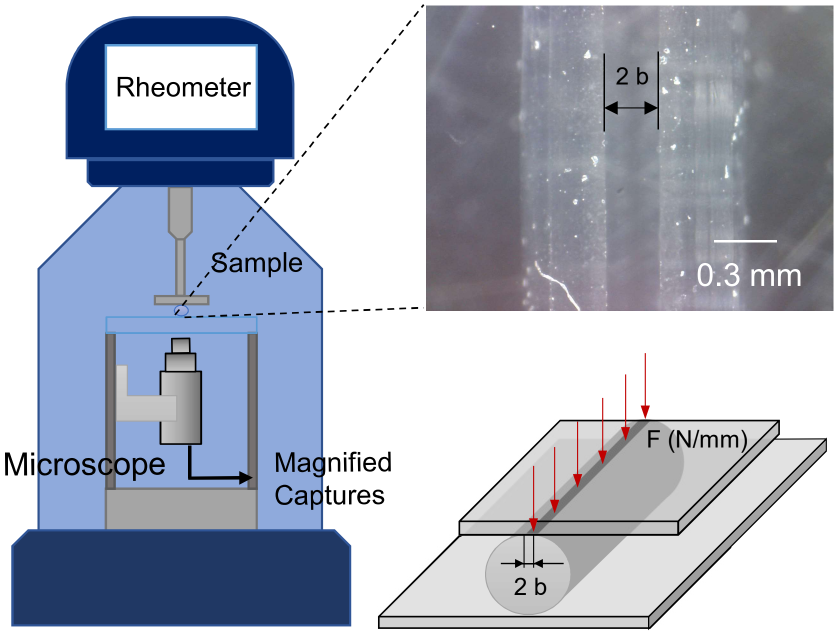

Figure 3.3: Radial modulus setup with the HR-2 and optics plate accessory (OPA)

$$b^2 = \frac{4FR}{\pi}(S_{22} + \frac{S_{21}}{S_{11}}) = \frac{4FR}{\pi}(S_{22} + \nu_{21}^2 S_{11}) = \frac{4FR}{\pi} S_{22}. \tag{3.4}$$

Equation 3.4 relates the half of the patch width, $b$, with the applied load per length, $F$, radius, $R$, and compliance in the radial direction, $S_{22}$. In addition, the term $\nu_{21}^2 S_{11}$ can be neglected because in drawn polymers the compliance in the axial direction, $S_{11}$, is very small compared with the compliance in the radial direction, $S_{22}$. Furthermore, the Possion's ratio is typically near 0.5 [50]. The second order nature of $\nu_{21}$ times $S_{11}$ makes this assumption reasonable. The final expression for the radial modulus (inverse of the compliance) is given by

$$E_2 = \frac{4FR}{\pi b^2}. \tag{3.5}$$

Figure 3.3 displays the layout for this test where the sample can be seen on top of a transparent optics plate accessory (OPA). Below, the microscope, which sits under the OPA captures images that are used to measure the patch width produced by a compression force applied by the mirrored flat plate attached to the head of the HR-2. Here, the OPA and digital microscope are attached to the HR-2. Under a prescribed displacement, the compressive force was recorded by the HR-2. Figure 3.3 also shows a 240x magnified photograph of a tested sample along with its patch width.

### 3.3.3 Poisson's ratio, $\nu_{12}$, setup

In the process of collecting the Poisson's ratio, radial and axial strains of the precursor monofilament were measured under a tensile load by a Keyence Digital Microscope. During this test, a few challenges were presented. The precursor monofilament has a cylindrical shape that does not allow to focus on the total width of the sample due to differences in distance between the focal lens and the cylindrical area. Thus, the tested samples were sanded to the midsection of the precursor monofilament, obtaining a flat surface as a result (Figure 3.4). After sample preparation, microscopic imperfections were identified at the midsurface, defined as referenced points and tracked by the microscope in the radial and axial directions. Measuring the change in position of the radial points is a challenging process, since displacement in this direction happens to be very small. A high tensile load was applied on the

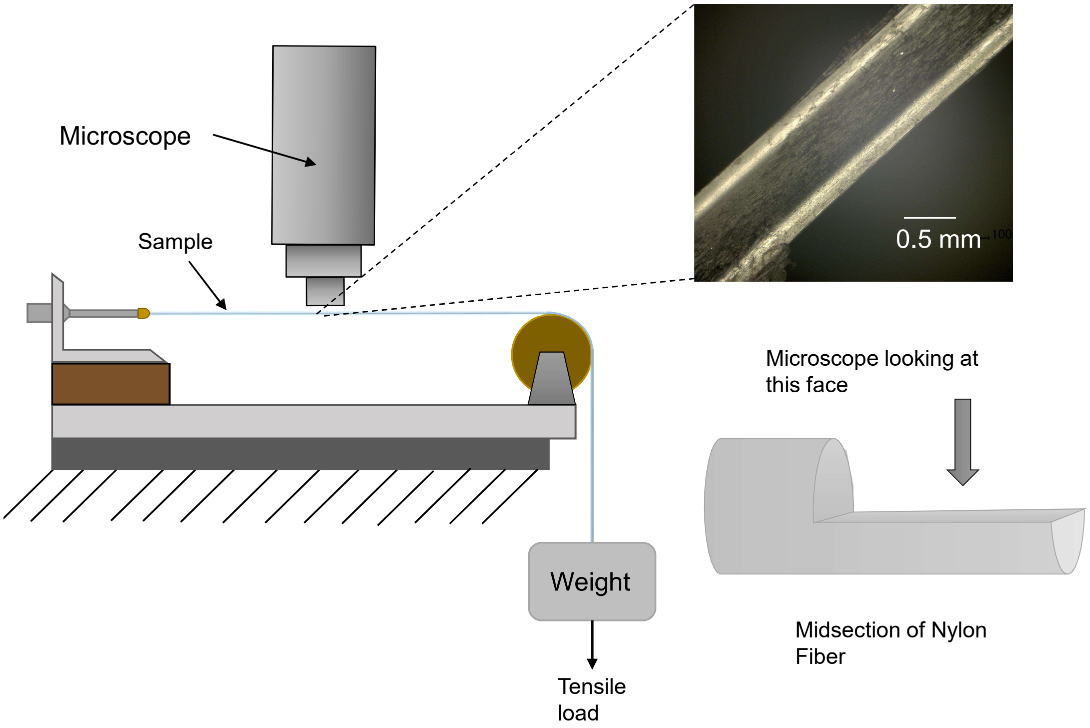

Figure 3.4: Posisson's ratio setup with Keyence Digital Microscope under a 300x magnification.

material to produce notable deformation in the radial direction.

Figure 3.4 displays a diagram of the Poisson's ratio setup where the sample is attached to a fixed point at one end and exposed to a tensile load at the other. The deformation produced by the mechanical load was recorded as a function of time in the radial and axial direction at the midsection of the precursor monofilament by using the Keyence Digital Microscope under a 300x magnification. Poisson's ratio, the ratio of radial to axial strain under axial load and is given by

$$\nu_{12} = -\frac{\varepsilon_{Radial}}{\varepsilon_{Axial}}. \tag{3.6}$$

### 3.3.4 Axial thermal contraction, $\varepsilon_{11}^{T}$, setup

The axial thermal contraction of the precursor monofilament was measured using three systems: the Polytec OFV-5000 Vibrometer controller with the OFV 534 optics head to measure displacement, the FLIR A300-Series thermal camera with an IR 10 mm focal lens to measure temperature, and the Sparkfun Electronics 303 D heat gun to manually control changes in temperature.

In previous experimental setups, the HR-2 with the ETC system was used to achieve axial thermal contraction characterization. However, the obtained results were called into question because quick changes in temperature were measured by a thermocouple placed at the perimeter of the ETC. So, after proof testing with a thermocouple near the sample, and external to the HR-2 system, it was shown that the ETC temperature measurements did not match with the temperature of the sample. In addition, temperature inputs as a function of time on the HR-2 system were not well controlled due to the thermal inertia of the system, thus rapid changes in temperature did not happen as expected, leading to overshooting and time lapses.

In an effort to solve these inaccuracies, a setup was found with the use of the thermal camera to measure temperature, the vibrometer to measure axial displacement, and the heat gun to control the temperature input (Figure 3.5(a)).

Figure 3.5(a) shows a 2 cm long sample vertically clamped by the top end to a fixed point and hanging freely at the bottom end with a 9 grams mass to ensure that the sample stays straight. The sample was heated using the Sparkfun Electronics 303D heat gun with an attached 30 cm long insulated copper tube. To ensure a consistent temperature over time and space the tube was preheated for 20 minutes

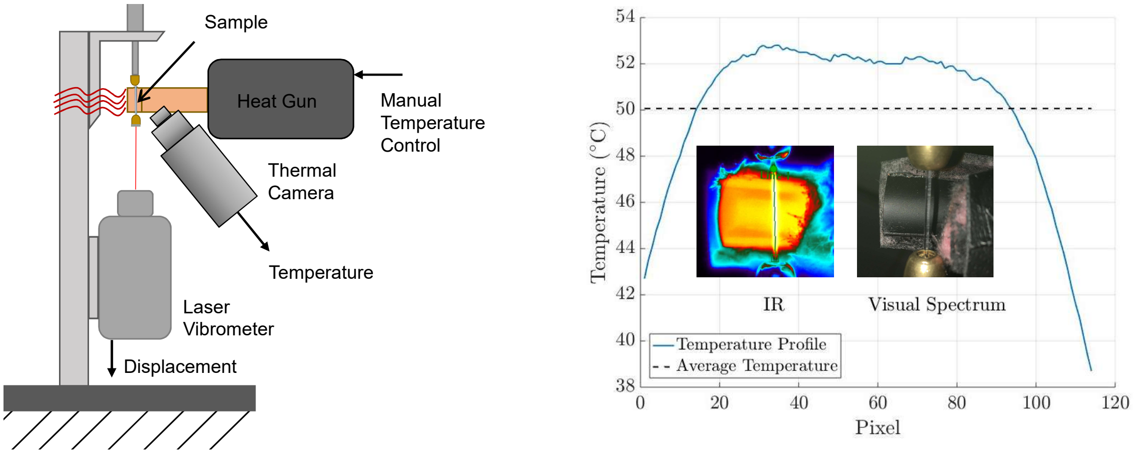

(a)

(b)

Figure 3.5: (a) Experimental setup for axial thermal contraction; (b) temperature profile of sample recorded by the thermal camera FLIR A300-Series under thermal loading from the Sparkfun Electronics 303D heat gun.

before running the test. A screen was inserted inside the copper tube to create a turbulent flow and a more uniform temperature profile (Figure 3.5(b)). The thermal camera was placed perpendicular to the sample and out of the flow stream of the heat gun to avoid damage. The vibrometer was positioned directly below the sample with the laser reflecting off the bottom of the attached mass at the end of the sample. Before testing the thermal axial contraction, a drift test was conducted on the vibrometer under the settings of 100 $\mu$m/V and fast tracking filter (same conditions used in the axial thermal contraction test), by focusing the laser on a fixed point on a bench for one and a half hours to ensure that the results achieve a steady state. After a warm-up time of 40 minutes and appropriate laser focusing, it could be assumed that the drift of the system was negligible. Figure 3.5(b) displays the average temperature along the sample, and it also displays an infrared image along with a photograph of the copper tube and sample.

### 3.3.5 Radial thermal expansion, $\varepsilon_{22}^{T}$, setup

Before addressing an experimental setup for measuring radial thermal expansion, it is worth mentioning that Aziz et al. have experimentally obtained radial thermal expansion data [2]. Aziz et al. calculate the radial thermal expansion by using the volumetric change of the precursor monofilament immersed in a test tube filled with silicon oil. This experiment was run from 26 to 62°C where the axial thermal contraction was assumed negligible. Consequently, the change in volume is entirely attributed to the radial thermal expansion and the expansion of the silicon oil, which had been measured and accounted for in calculations of radial expansion. They performed these tests with both STPAs and precursor monofilaments (i.e. twisted and untwisted samples) and found no difference in the radial thermal expansion.

Aiming to imitate the Aziz et al.'s liquid immersion setup, a similar experiment was conducted in our laboratory. During this test, a few concerns were observed:

- The precursor monofilament's tendency (Section 3.2.1) to absorb moisture could potentially change the expansion properties of the material.
- Vapor bubbles emigrated from the samples during the heating process (Figure 3.6).
- Bubbles appeared within mineral oil appeared at temperatures close to a 100°C (Figure 3.7) and were assumed to be escaping moisture from within the material sample.

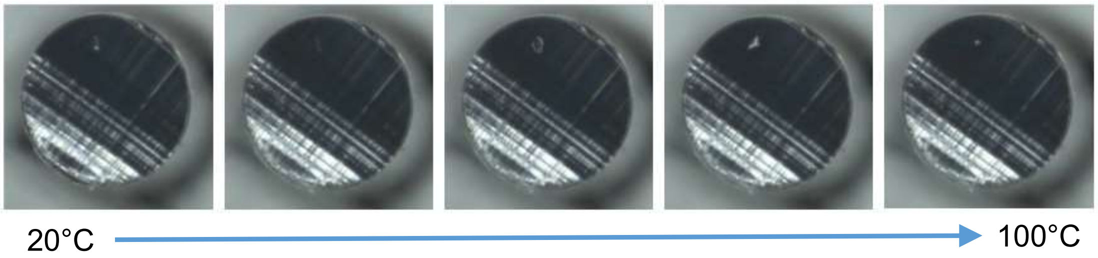

Figure 3.6: Emigration of a vapor bubble from the inside of the precursor monofilament.

It should be noted that these tests were conducted prior to the development of the dessication protocol. In addition, it also needs to be considered that for temperatures higher than 62°C, axial thermal contraction occurs, so it is not valid to neglect changes in sample length.

In an effort to remove these experimental errors, a new experimental layout for radial thermal expansion was found by using a Keyence Digital Microscope and the TE Technologies CP-031HT cold plate cooler with the TC-720 temperature controller to control the temperature input and collect temperature data (Figure 3.8).

After sample preparation (desiccation and pre-cycling thermally), the precursor monofilament was cut into slices of approximately 0.5 mm thick using a microtome blade. As a result, flat faces with identifiable marks close to the edges, could be used as references for measured points during heating and cooling. Figure 3.8 displays the sample set onto the cold plate, which transfers heat to the sample, while the surrounding sides were isolated by fiber glass and enclosed on the top by the head of the microscope. Images of the flat faces were recorded to measure dimensional changes in the radial direction by the microscope under a 300x magnification, while

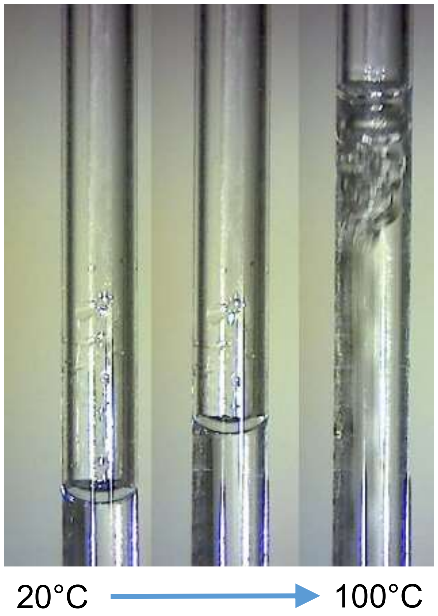

Figure 3.7: Bubbles produced by the imcrement of temperature to 100°C.

increasing the temperature from room temperature to 95°C.

The temperature was acquired by a thermistor attached to the cold plate. Calibration of the thermistor was required because it records temperature of the cold plate, which was found to not accurately match the temperature of the sample. During this calibration test, the thermal camera was used as the corrected reference temperature. As the setup shown in Figure 3.8, a similar setup was established during calibration where the thermal camera substitutes for the microscope. Temperature was recorded as a function of time by the thermal camera and the thermistor simultaneously, then both sets of data were plotted to find a calibration fit (Figure 3.9).

Two different calibration fits were required, one for the radial thermal creep

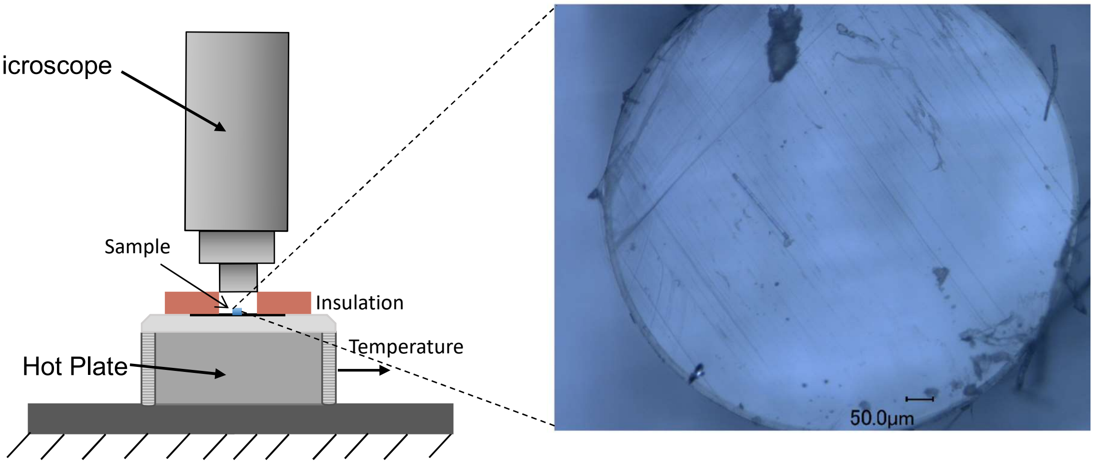

Figure 3.8: Radial thermal expansion coefficient setup with a 300x magnified photo.

test (Figure 3.9(a)) and a second one for the radial thermal expansion test (Figure 3.9(b)). The former uses a temperature pulse then hold to allow for thermal creep, while the latter has a slower ramp of temperature with time so that strains can be measured during heating/cooling. Figures 3.9(a) and 3.9(b) display the control temperature (i.e. the input for the cold plate) along with the temperature results of the thermistor and thermal camera as a function of time. A fourth calibrated function has been included wherein the data from the thermistor was translated is correct by a calibration amount to match that from the thermal camera.

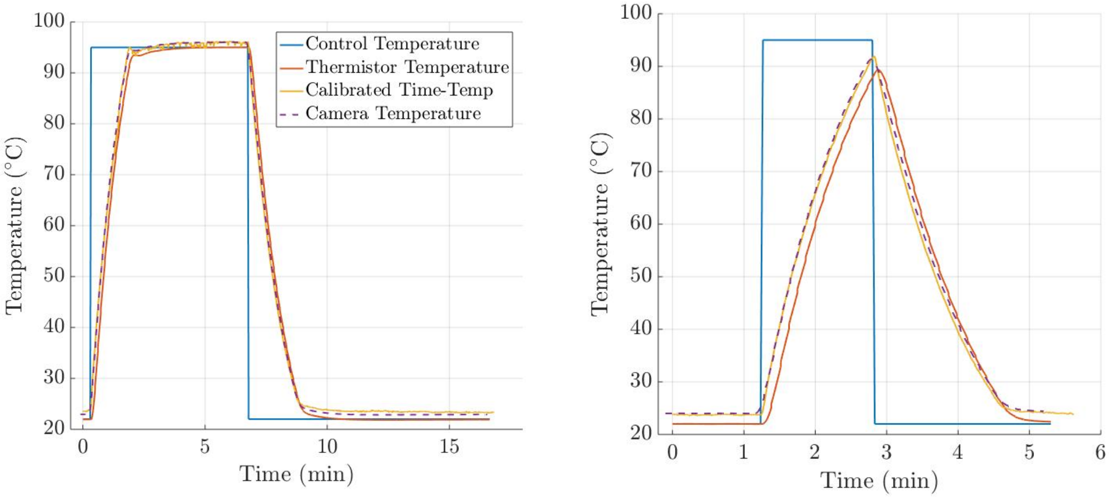

(a)

(b)

Figure 3.9: (a) Cold plate calibration for the radial thermal creep test; (b) cold plate calibration for the radial thermal expansion test.

## 3.4 Experimental methods and results

In this section, I present the experimental methods and results for the following properties: axial modulus, $E_1$, shear modulus, $G_{12}$, radial modulus, $E_2$, Poisson's ratio, $\nu_{12}$, axial thermal contraction, $\varepsilon_{11}^T$, and radial thermal expansion, $\varepsilon_{22}^T$. As previously discussed, $\nu_{23}$ is assumed to be that for bulk nylon 6,6, and thus $\nu_{23}$ is equal to 0.41 [51].

### 3.4.1 Axial modulus, $E_1$

In most TPA applications [1], tensile loads are applied on the coiled monofilament, such as a bias mass applied at the end of a TCPA that is lifted as a result of the actuation. Furthermore, a low tensile load might exist in STPA applications to keep the actuator straight [34, 3]. The total strains in this actuators are the addition of thermal strains and mechanical strains

$$\varepsilon_{11}^{Total} = \varepsilon_{11}^{Mechanical} + \varepsilon_{11}^{Thermal} = \frac{1}{E_1}\sigma + \alpha_{11}T. \tag{3.7}$$

The mechanical strain is often calculated as a relationship of stress and a material property, like Young's modulus, $E_1$, for linear elastic materials as in Equation 3.7. In modeling these active actuators, characterization of the axial modulus is needed for actuation models under tensile loads.

In this section, I approach the elastic axial modulus for different steady state temperatures and the axial modulus as a function of time to characterize the viscoelastic effects.

### Elastic axial modulus as a function of temperature

In this experiment, linear elastic behavior as a function of temperature was assumed. For this test, the sample was thermally pre-cycled for five thermal cycles at 110°C for two minutes and cooled to room temperature by free convection. Then, a 2 cm long sample was placed in the HR-2, and a strain of 1% was applied over ten 10s cycles at room temperature (mechanical pre-cycle). Prior to this experiment, the 1% strain was tested to be inside the elastic region of deformation by running the same stress-strain curve for a higher deformation and making sure that this value did not yield plastic deformation.

A total of five stress-strain experiments were conducted for different temperatures: 25°C, 45°C, 65°C, 85°C, and 105°C. All tests were done in displacement control mode up to approximately 1 %. The loading rate for all tests was 1 %/min. For those experiments above room temperature the first cycle effects were still present, even though the samples were mechanically and thermally pre-cyled. In order to eliminate first cycle effects in these tests, three more cycles at the prescribed temperature were conducted. After these cycles, stress-strain results seemed to converge (Figure 3.10(a)).

Figure 3.10(b) displays the results for the last converged cycles, it can be seen that the elastic axial modulus falls as the temperature rises. Even though hysteresis is notable, a linear fit was used to calculate the axial modulus, $E_1$, from these curves. The slight hysterertic behavior due to the viscoelastic properties of the precursor monofilament can induce inaccuracy in the prediction of the stress-strain relationship. Figure 3.10(c) shows the elastic axial modulus, $E_1$, as a function of temperature observed in Figure 3.10(b), which can be fit by the following cubic equation

$$E_1(T) = -8.2 \times 10^{-6}\, T^3 + 0.003\, T^2 - 0.24\, T + 8.31, \tag{3.8}$$

where T is temperature in Celsius.

### Time-dependency and viscoelastic behavior of the axial modulus

When finding the viscoelastic parameters, two different test can be conducted: relaxation stress and mechanical creep. The one that has been used for obtaining the viscoelastic parameters is the relaxation stress because the expression used to fit this results are considerably simpler that the one for the creep tests.

A thermally pre-cycled sample of approximately 2 cm was subjected to an axial

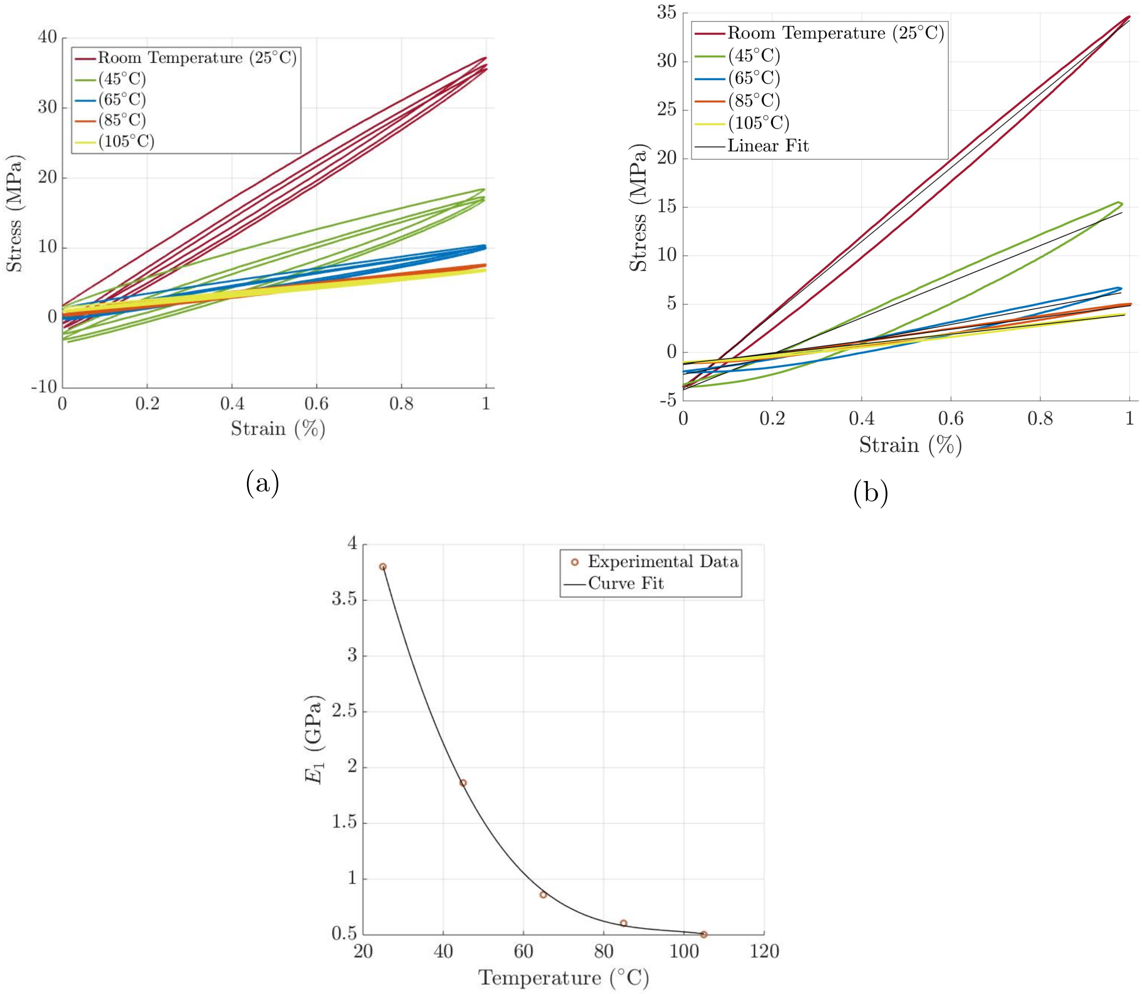

(a)

(b)

(c)

Figure 3.10: (a) Three cycles of the stress-strain curves at the defined temperatures; (b) stress-strain curves for the last cycle at different steady state temperatures; (c) elastic axial modulus as a function of temperature

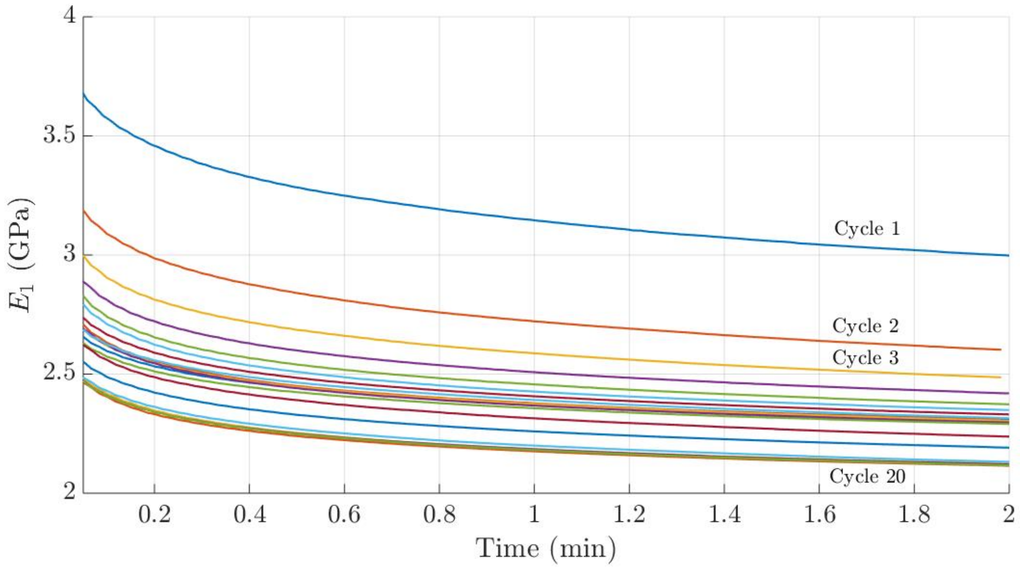

Figure 3.11: Axial modulus as a function of time for a total of 20 cycles.

load of 22 N (35 MPa). During this experiment, overshooting occurred and the loads varied for different cycles. Similarly, recovery cycles were set by reducing the load to less than 1 N ($\leq$ 0.4 MPa). The experiment was conducted for a total of 20 cycles where the first 19 cycles lasted four minutes (two minutes in which the material was held at the highest load and two minutes in which the material was held at the lowest load) and a final cycle in which the material was held for 20 minutes at the highest load. This last cycle was used to calculate for viscoelastic parameters.

Figure 3.11 shows a total of 20 cycles where a significant relaxation was found. Convergence occurred at cycle number 12; however, right after this cycle the subsequents results for, $E_1$ dropped again. This is because the mechanical loading during the experiment was unstable due to the rheometer controller issues. For the first 12 cycles, the maximum load was between 50 and 40 MPa, but after the fifteenth cycle

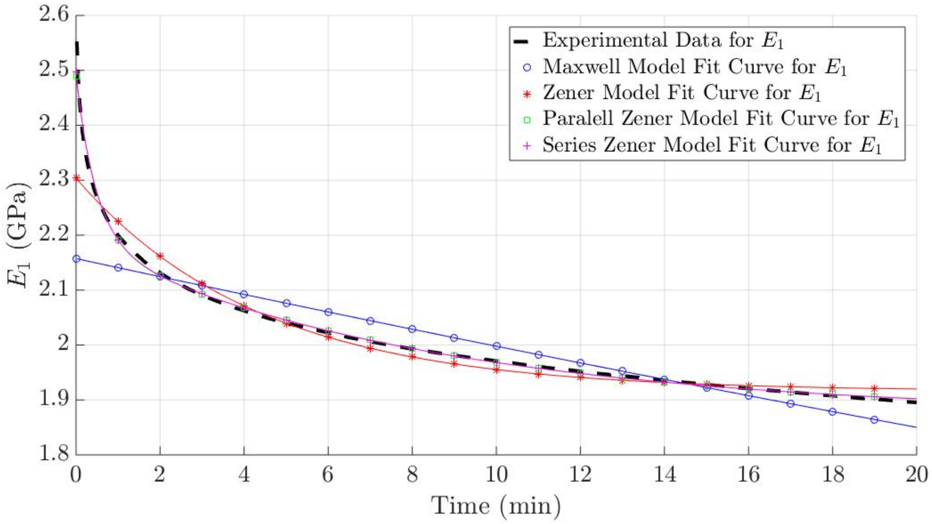

Figure 3.12: Viscoelastic fits for the last converged cycle.

the maximum load changed to a range between 50 and 60 MPa. Future work should address this imprecision. However, the issues with the rheometer controller show the Mullin's effect, because there is a new first cycle effect of the material when a higher mechanical load was applied.

Figure 3.12 shows how the four viscoelastic models: Maxwell, Zener, improved parallel, and improved series Zener with two spring-dash elements, fit the final cycles of the axial stress relaxation data. The best fit was found for the improved parallel or series models with two spring-dash elements. The combination of two spring-dash elements allows the viscoelastic model to capture the initial and final exponential response of the material. The mathematical expression for each model are

- Maxwell model

$$E_1(t) = 2157e^{-t/7811}. \tag{3.9}$$

- Zener model

$$E_1(t) = 1916 + 387.8\ e^{-t/262.2}. \tag{3.10}$$

- Improved parallel Zener model with two dashpot-spring elements

$$E_1(t) = 1875 + 300.8\ e^{-t/29.53} + 312.9\ e^{-t/496.4}. \tag{3.11}$$

- Improved series Zener model with two dashpot-spring elements

$$E_1(t) = \left(\frac{1}{2313} + \left(\frac{1}{3.96 \times 10^{10}}\right)e^{-t/-577.8} + \left(\frac{1}{1.108 \times 10^{4}}\right)e^{-t/289.4}\right)^{-1}. \tag{3.12}$$

In all cases, t is the time in minutes.

### 3.4.2 Shear modulus, $G_{12}$

The shear modulus (modulus of rigidity), $G_{12}$, is a property used to determine the behavior of the material under a shear stress. Similar to axial behavior, the shear stress-strain relationship is affected by time due to viscosity of the material, thus a viscoelastic model was required for characterization of the material. Also, like the axial behavior, I examine how the linear elastic shear modulus changes with temperature.

### Elastic shear modulus as a function of temperature

The methodology of this test is similar to the one explained in the $E_1$, (Section 3.4.1), where the sample was set between the clamps of the torsional accessory in the HR-2 under a torsional load equal to 5 N mm with a load rate of 5 N mm / min, producing a shear strain in the elastic region. This experiment was conducted for different steady state temperatures applied by the ETC, while collecting torque and angular displacement data in order to calculate the shear modulus as a function of time.

The sample was thermally pre-cycled for five thermal cycles of four minutes each (two minutes at 110°C and two minutes at room temperature) along with ten 10s mechanical cycles at room temperature, where the tested torsional load of 5 N mm was applied to the sample. A total of five experiments were run for the following temperatures: 25°C, 45°C, 65°C, 85°C, and 105°C. For temperatures above room temperature a total of three more cycles had to be conducted at the specified temperature in order to obtained converged results because the first cycle effect still appeared even after initial cycling.

Figure 3.13(a) displays the shear stress-strain curves for the final cycle at each temperature. Note that a hysteretic response is detected, and the hysteresis increases as the temperature rises. This behavior is likely due to the fact that for higher temperatures, polymers tend to become more viscoelastic. Even though hysteresis was present, a linear fit was still applied under the assumption of elastic response. For each curve a shear modulus was found and plotted as a function of temperature in Figure 3.13(b). Predictions of the elastic shear modulus in terms of temperature

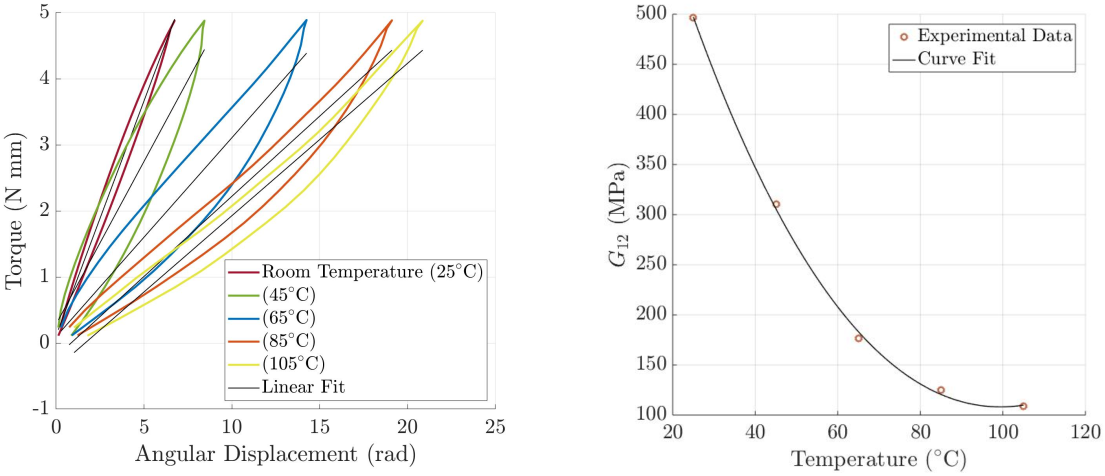

(a)

(b)

Figure 3.13: (a) Torque-Agular displacement plots at different temperatures; (b) elastic shear modulus a function of temperature.

in a range between 20°C and 110°C are given by

$$G_{12}(T) = -0.00017\ T^3 + 0.109\ T^2 - 16.56\ T + 845.65 \tag{3.13}$$

where T is temperature in Celsius.

### Time-dependency and viscoelastic behavior of the shear modulus

To determine the time-dependent behavior of $G_{12}$, a 2 cm sample was set in the HR-2, where the torsional displacement was initialized to zero and the axial tensile load was 0.1 N to ensure that the sample did not buckle. The sample was twisted and held at a torsional displacement of $\pi$ radians for 20 minutes. Then, the sample was taken to the initial position of 0 radians and held for the same period of time to allow for recovery. A total of five loading and unloading cycles were run.

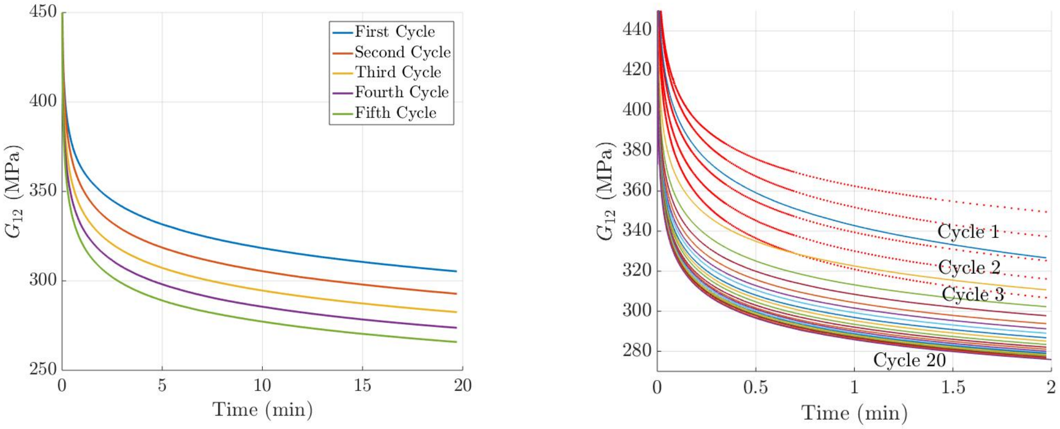

(a)

(b)

Figure 3.14: (a) First shear modulus test for a total of five cycles; (b) Second shear modulus test for 20 cycles.

Figure 3.14(a) shows the shear modulus as a function of time for the five cycles. The shear modulus becomes fairly constant after 15 minutes yet, convergence does not occur for the first five cycles. In these results, the data was cropped for the first tenth of a second because the shear modulus went to infinity due to a zero angular displacement.

In order to find converged results, a second test was conducted where a total of 20 cycles were run. To reduce the testing time, the first 19 cycles had a duration of four minutes (two minutes loading and two minutes unloading) and the final cycle is run for a total of 20 minutes. Figure 3.14(b) shows the 20 cycles, where convergence occurs faster than in the previous test (Figure 3.14(a)). This effect is potentially due to the shorter recovery time. The shear modulus converges after 15 cycles and the final cycle was used to calculate viscoelastic parameters.

As with previous time-dependent properties, fits have been used to characterize

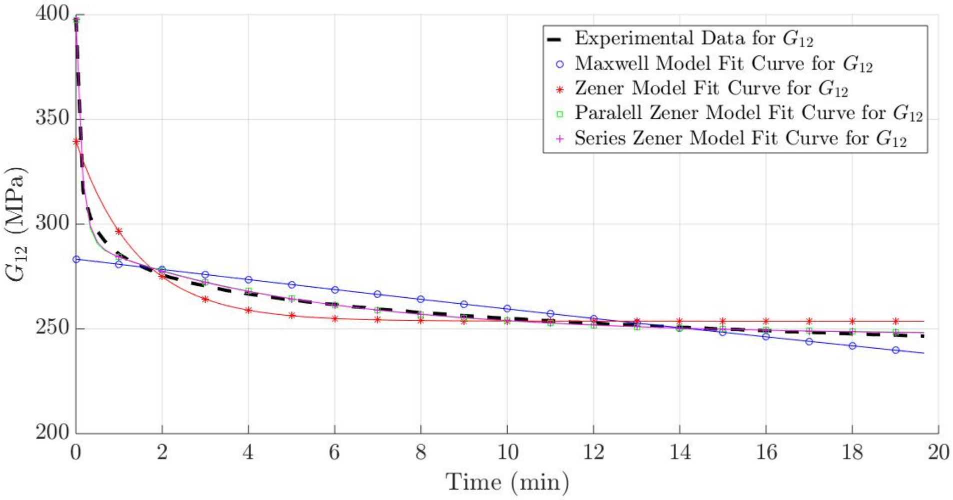

Figure 3.15: Viscoelastic fits for the last converged cycle.

the viscoelastic parameters of the $G_{12}$ (Figure 3.15). The best fit was found to be the improved parallel and improved series Zener models with two spring-dash elements. The viscoelastic fits for each model are

- Maxwell model

$$G_{12}(t) = 283.3e^{-t/6839}. \tag{3.14}$$

- Zener model

$$G_{12}(t) = 253.7 + 85.89\ e^{-t/85.88}. \tag{3.15}$$

- Improved parallel Zener model with two dashpot-spring elements

$$G_{12}(t) = 247.4 + 105.3\ e^{-t/7.964} + 44.82\ e^{-t/309.8}. \tag{3.16}$$

- Improved series Zener model with two dashpot-spring elements

$$G_{12}(t) = \left( \frac{1}{397.7} + \left( \frac{1}{1105} \right) e^{-t/9.577} + \left( \frac{1}{1583} \right) e^{-t/350.5} \right)^{-1}. \tag{3.17}$$

In all cases, t is the time in minutes.

### 3.4.3 Radial modulus, $E_2$

In this section, experimental methods and results are presented for the time-dependent of the radial modulus. The temperature dependence has not been studied in this work because this property is experimentally difficult to obtain as a function of temperature; however, the linear elastic radial modulus as a function of temperature is expected to follow the same behavior as presented in Equations 3.8 and 3.13 for axial modulus and shear modulus, respectively.

#### Time-dependency and viscoelastic behavior of the radial modulus

As it was explained in Section 3.3.2, the radial modulus was experimentally obtained by the methodology presented in the book Mechanical Properties of Solid Polymers [50]. In this experiment the precursor monofilament was located between the OPA and the flat mirrored plate of 4 cm in diameter. The tested sample was cut with a length of 6.75 mm; this length was found to be suitable in order to ensure enough pressure on the specimen to produce a measurable patch, as well as meet the aspect ratio requirement of L>D, for the plane strain assumption.

After setting the sample in place, a script was written to run a total of five

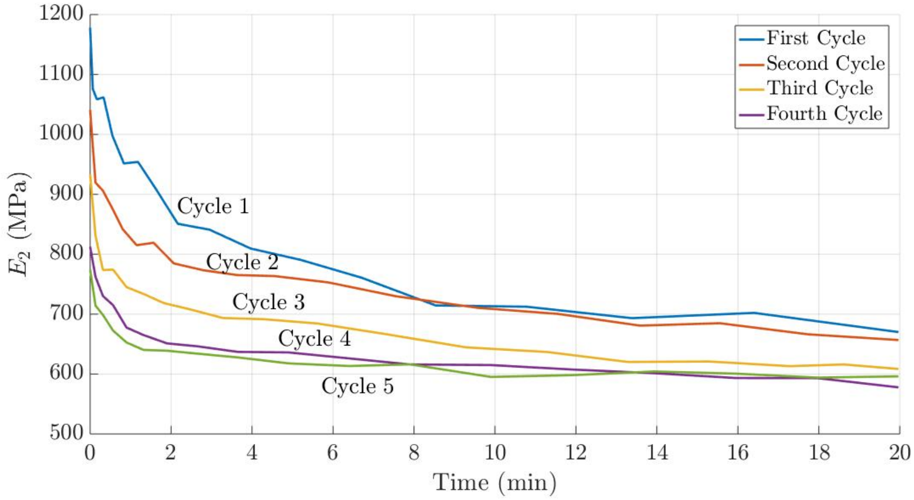

Figure 3.16: Radial modulus as a function of time for five cycles

transversally compressive cycles. In this experiment, the gap between plates was set to be 0.57 mm and held constant for 20 minutes after a step function input. The compressive force, $F_c$, was recorded by the HR-2 and the patch, 2b, was filmed by the digital microscope. During the test, the patch of the sample was growing as a function of time. Furthermore, $F_c$ dropped due to the relaxation of the precursor monofilament.

Figure 3.16 shows the time-dependent response for $E_2$ to be constant after 15 minutes; however, it also displays a first cycle effect, where the first three cycles scaled down without showing convergence. The fourth and fifth cycles aligned and convergence or near convergence seems to be a reasonable assumption.

Figure 3.17 shows the four viscoelastic models: Maxwell, Zener, improved parallel, and improved series Zener with two spring-dash elements, as compared to experimental data for $E_2$ from the last cycle. The improved parallel and improved series Zener models with two spring-dash elements were found to suitable capture

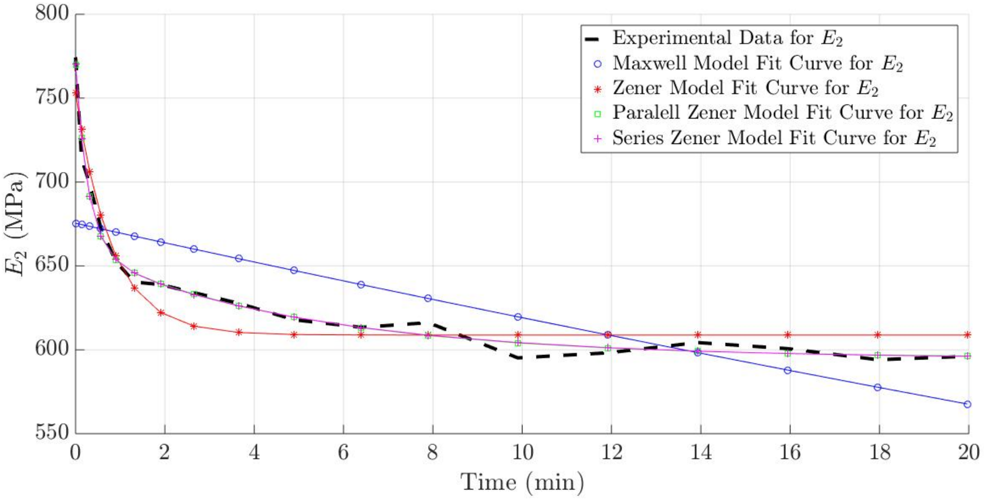

Figure 3.17: Viscoelastic fits for the fifth cycle.

the viscoelastic response of $E_2$. The combination of two spring-dash elements allows the viscoelastic model to fit the initial and final exponential response of the material.

As found for other mechanical properties, the parallel Zener model with two elements capture the viscoelastic response the best. The viscoelastic mathematical expression for each model are given by

- Maxwell model

$$E_2(t) = 675.4e^{-t/6893}. \tag{3.18}$$

- Zener model

$$E_2(t) = 608.8 + 144.6\ e^{-t/48.16}. \tag{3.19}$$

- Improved parallel Zener model with two dashpot-spring elements

$$E_2(t) = 595.1 + 64.5\ e^{-t/301.5} + 110.1\ e^{-t/16.91}. \tag{3.20}$$

- Improved series Zener model with two dashpot-spring elements

$$E_2(t) = \left( \frac{1}{770.4} + \left( \frac{1}{6049} \right) e^{-t/327.5} + \left( \frac{1}{4577} \right) e^{-t/18.72} \right)^{-1}. \tag{3.21}$$

In all cases, t is the time in minutes.

### 3.4.4 Poisson's Ratio, $\nu_{12}$

The test described in Section 3.3.3 was use to find Poisson's ratio as a function of time. Since axial and radial moduli are time-dependent, Poisson's ratio is expected to be as well. Even though Poisson's ratio as a function of temperature is not presented in this research, it might be of interest in future works.

#### Time-dependent behavior of the Poisson's ratio

Small changes to strain in the radial direction made the referenced imperfections very difficult to track, and yielded high variability in the data, as can be seen in Figure 3.18, which shows the results of Poisson's ratio after applying an axial mechanical load of approximately three kilograms. The data oscillate for the first ten minutes. It is unclear if this error was human measurement error or actual variations in the material. After 15 minutes, the results become more stable since the viscoelastic effects reach steady state. The result for the Poisson's ratio shows an average of 0.304.

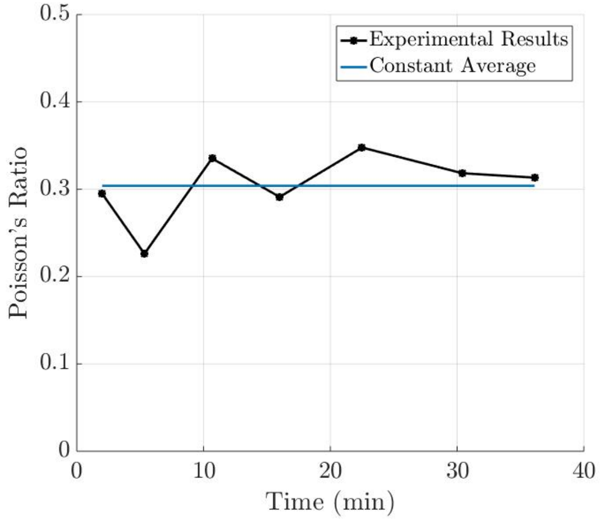

Figure 3.18: Poisson's ratio as a function of time.

### 3.4.5 Axial thermal contraction, $\varepsilon_{11}^{T}$

Dimensional changes in the axial and radial directions are considered to be the driving forces of actuation in TPAs [3, 2, 1]. In this section, dimensional changes in the axial direction of the precursor monofilament are presented as a function of temperature. I also consider the time-dependent behavior of this thermal property in order to analyze how viscous effects in the material are manifested under thermal load. For this test, the tested precursor monofilaments have not been thermally precycled, so first cycles effects will be visible in the results.

#### Time-dependency and Viscoelastic Behavior of the Axial Thermal Contraction

Prior to collecting the thermal axial contraction data, an experimental test for thermal creep was conducted with the purpose of finding the time-dependencies of axial thermal strain. If notable changes in thermal axial contraction occur as a function of time, then the axial thermal strain will need to be modeled as a function of time. Note that the axial thermal contraction experiment look approximately four minutes to run, thus viscous effect could potentially change the observed axial thermal contraction.

The setup for axial thermal contraction was explained in Section 3.3.4. For the time dependent tests, quick ramps of temperature were applied, followed by maintaining the temperature in order to detect thermal creep symptoms. Figure 3.19 displays the temperature ramp used, which includes a total of five completed cycles of approximately 45 minutes each, (20 minutes at a high temperature and 25 minutes at room temperature). The temperature change is quite quick, ramping from room temperature ($\sim$ 22°C) to approximately 90°C in 40 seconds and reverse in 50 seconds.

The axial strain in Figure 3.19 shows that the first cycle behaves quite differently than subsequents cycles. As previously mentioned, this first cycle effect has been well documented for tests under mechanical loads [48]; however, no literature has been found in this matter under thermal expansion measurements. After the first cycle, the subsequent cycles show full recovery, (Figure3.19), although axial thermal creep was still observed. As the temperature is held constant at approximately 90°C and room temperature the axial thermal strains change with time. Even though thermal creep occurred, the rate of creep was relatively slow and consistent in behavior and magnitude. An average of thermal creep was calculated at room temperature ($\sim$ 22°C) and 90°C, being 0.001 %/min and -0.0015 %/min, respectively. The average

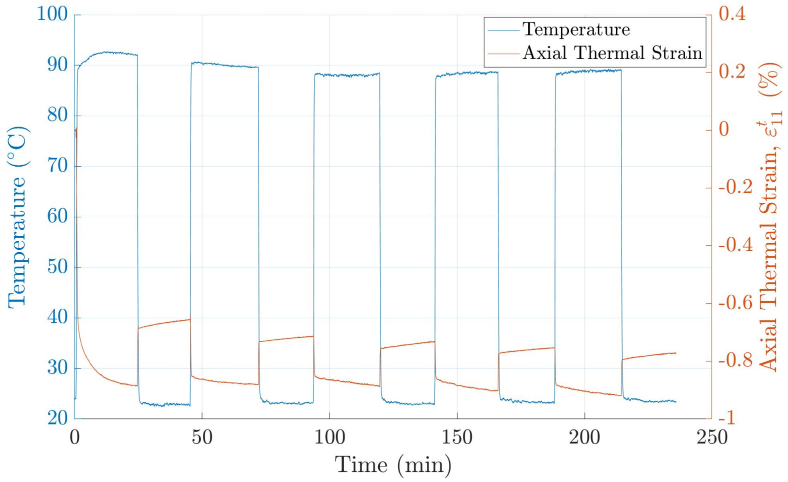

Figure 3.19: Thermal strain and temperature as a function of time for a total of five cyles.

magnitude of the axial thermal strain temperatures was 0.132 %; thus, the average rate of creep was approximately 1 %/min of the total thermal strain. Since the axial thermal contraction results were conducted by a temperature ramp lasting two minutes, for heating and cooling, it can be said that for short term experiments where actuation occurs in quick periods of time ($\lesssim$ 6 minutes), the thermal creep is negligible.

### Thermal axial contraction as a function of temperature

For this test a total of six cycles were conducted because previous experiments (e.g. Figure 3.19) showed a considerable first cycle effect and that the samples had not be pre-cycled. All cycles were run in the same manner as the thermal creep experiment, where the temperature was manually controlled by the heat gun to be linearly ramped up to 100°C and down to room temperature with the same rate of change

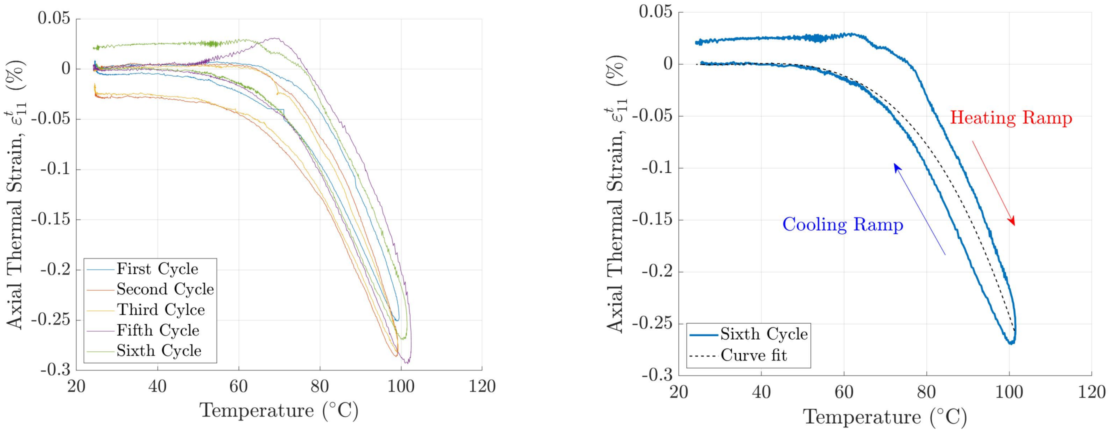

(a) (b)

Figure 3.20: (a) Axial thermal contraction for six thermal ramps; (b) axial thermal contraction for the last cycle

of temperature. The heating and cooling times were two minutes, thus a complete cycle was conducted every four minutes.

As mentioned, the change in position was obtained by the vibrometer under the settings displacement conversion of 10 $\mu$m /V and a fast tracking filter. The displacement data was recorded in a LabVIEW script as a function of time. Temperature and the time were collected by the thermal camera.

Figure 3.20(a) shows the results from the thermal contraction test. In these results, the fourth cycle is missing because the data was not recorded. A “first cycle effect” was observed, but the cycles two and three converge. During this test, it was seen that the emissivity of the tube of the heat gun behind the samples was skewing the temperature measurements by a few degrees Celsius. The interior of the tube was painted in black for cycles five and six, shifting the results of these cycles slightly to the right. The fifth cycle shows a discrepancy in the final results, potentially because

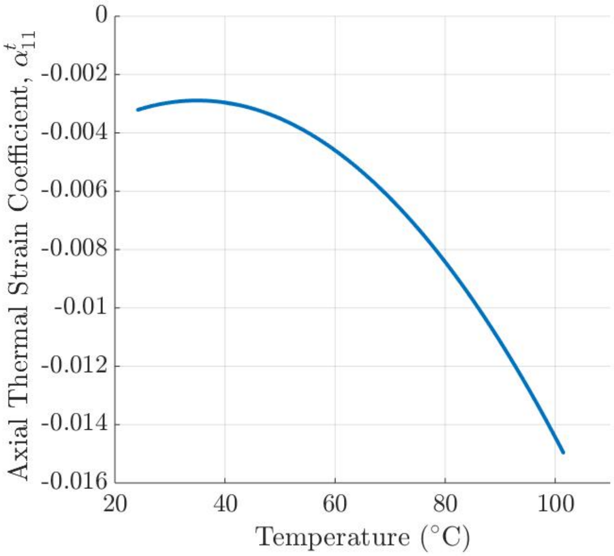

Figure 3.21: Axial thermal contraction coefficient.

of incorrect aiming of the vibrometer laser; however, cycle number six displays good qualitative and quantitative results that were used to calculate the axial thermal contraction coefficient.

Hysteresis appeared in these results, since thermal creep was found to occur in the time range that this experiment was conducted. Even though hysteresis is presented, it was neglected to create a curve fit for the sixth cycle, which is shown in Figure 3.20(b) and given by

$$\varepsilon_{11}^{T} = [-0.0091(T^3 - T_0^3) + 0.954(T^2 - T_0^2) - 32.1(T - T_0)] \times 10^{-4}. \tag{3.22}$$

The axial thermal expansion coefficient can be obtained by differentiating Equation

3.22. The result is shown in Figure 3.21 and given by

$$\alpha_{11}^{T} = [-0.0273(T^2 - T_0^2) + 1.91(T - T_0) - 32.1] \times 10^{-4}. \tag{3.23}$$

where variable $\alpha_{11}^{T}$ is the slope of the thermal axial contraction and parameter often used for actuation models. In Equations 3.22 and 3.23, $T$ is temperature in Celsius and $T_0$ is an arbitrary reference temperature in Celsius.

### 3.4.6 Radial thermal expansion, $\varepsilon_{22}^{T}$

In previous research [2, 1], it has been claimed that radial thermal expansion is significantly greater than the axial thermal contraction in drawn monofilaments used to make TPAs, resulting in this property being the primary driving force of actuation. In this section, quantitative and qualitative experimental results for radial thermal expansion and viscoelastic behavior are presented.

#### Time-dependency and viscoelastic behavior of the radial thermal expansion

The radial thermal creep was obtained using the radial thermal expansion setup described in Section 3.3.5. Pre-cycled samples were placed onto the cold plate and subjected to 30 minutes at high temperature (95°C) and 30 minutes at low temperature (22°C). During this time, pictures of the sample were taken by the digital microscope and the temperature was recorded by the cold plate thermistor as corrected as described in Section 3.3.5. The change in the radial strain and the corrected

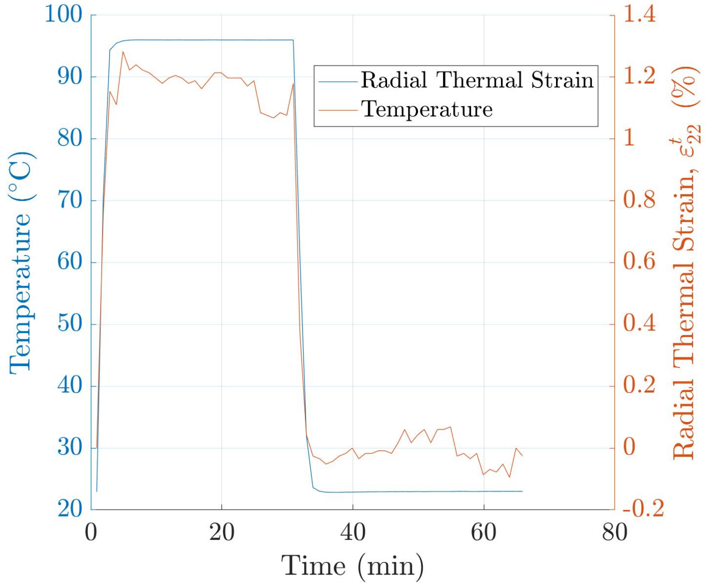

Figure 3.22: Radial thermal creep.

temperature are plotted as a function of time in Figure 3.22. In this figure, it can be seen that the thermal strain results oscillate in a range of 1.2 ± 0.1 % at high temperature and 0 ± 0.1 % at room temperature. Even though aleatory error was presented, thermal creep was not observed.

### Thermal radial expansion as a function of temperature

Figure 3.23 shows the experimental results for the radial thermal strain as a function of temperature. The results were obtained using a linear temperature ramp that lasted approximately four minutes (two minutes heating and two minutes cooling), and occurred after the thermal cycling for Figure 3.22. During cooling and heating ramps the thermal strain correlate well; minor offsets are likely due to human error, when measuring the change in strain. Some hysteresis is observed but it is consider

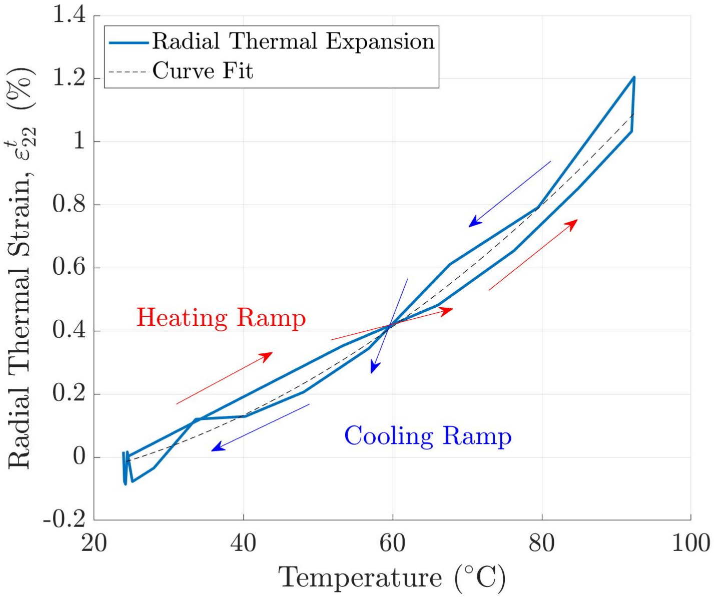

Figure 3.23: Radial thermal expansion.

negligible. The radial thermal strain can be fit by the quadratic curve in Figure 3.23 and given by

$$\varepsilon_{22}^{T} = [1.31(T^2 - T_0^2) + 9.29(T - T_0)] \times 10^{-4} \tag{3.24}$$

where $T$ is temperature in Celsius and $T_0$ is an arbitrary reference temperature in Celsius. In order to calculate the radial thermal expansion coefficient, the derivative of this equation is taken with respect to temperature, which yields

$$\alpha_{22}^{T} = [2.62(T - T_0) + 9.29] \times 10^{-4} \tag{3.25}$$

where $T$ is temperature in Celsius and $T_0$ is an arbitrary reference temperature in Celsius, also shown in Figure 3.24.

Comparing these results with the radial thermal strain results in Figure 3.23 to

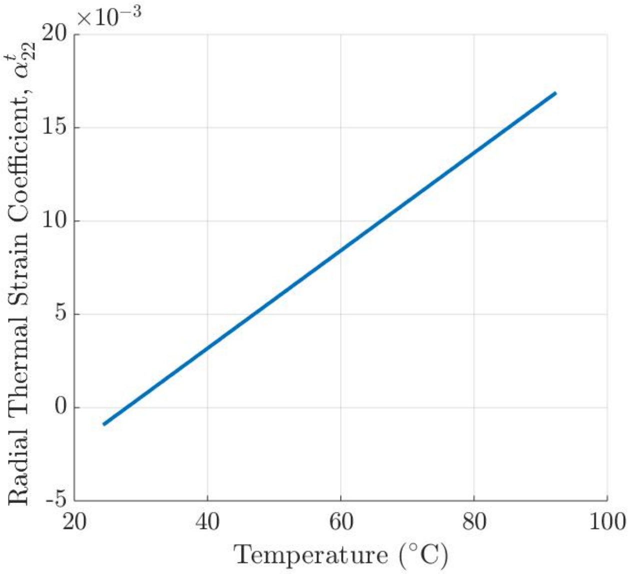

Figure 3.24: Radial thermal contraction coefficient.

those previously reported by Aziz et al. [2], they differ drastically. Aziz et al. claims nearly 2% strain at 60°C, but at that temperature, the strain in this experiment is less than 0.5%. Although Aziz et al. used the radial expansion of twisted specimens similar results were expected, as they showed no variation in radial expansion with increasing twist. Furthermore, it is not known what type of drawn polymer they have been used for the calculation of thermal radial expansion and different manufacturing techniques would affect the microstructure, resulting in differences in thermal expansion results. Additionally, the differences in these results could also be explained by the different experimental setups, since Aziz et al. used samples soaked in silicone oil, and moisture content can potentially affect the material properties.

## 3.5 Summary for Properties

Table 3.1: Summary of properties

| **Properties of the precursor monofilament** | **Characterization as a function of temperature (Elastic assumption)** | **Characterization as a function of time (Viscoelastic assumption)** |
|---|---|---|
| $E_1$ (GPa) | $E_1(T) = -8.2 \times 10^{-6}\ T^3 + 0.003\ T^2 - 0.24\ T + 8.31$ | $E_1(t) = 1875 + 300.8\ e^{-t/29.53} + 312.9\ e^{-t/496.4}$ |
| $E_2$ (MPa) | Not Found | $E_2(t) = 595.1 + 64.5\ e^{-t/301.5} + 110.1\ e^{-t/16.91}$ |
| $G_{12}$ (GPa) | $G_{12}(T) = -0.00017\ T^3 + 0.109\ T^2 - 16.56\ T + 845.65$ | $G_{12}(t) = 247.4 + 105.3\ e^{-t/7.964} + 44.82\ e^{-t/309.8}$ |
| $\nu_{12}$ | Not Found | $\nu_{12}(t) = 0.304$ |
| $\alpha_{11}^T$ (%/°C) | $\alpha_{11}^T(T) = (-0.0273\ (T^2 - T_0^2) + 1.91\ (T - T_0) - 32.1) \times 10^{-4}$ | N/A |
| $\alpha_{22}^T$ (%/°C) | $\alpha_{22}^T(T) = (2.62\ (T - T_0) + 9.29) \times 10^{-4}$ | N/A |

## Chapter 4

# Experimental Actuation of TPAs

In this chapter, I present experimental actuation data as well as experimental methods for different test conditions: free torsional actuation and torsional actuation under an isotonic torsional load. The isotonic load tests included both single monofilament and parallel STPA configuration actuation.

## 4.1 Fabrication of torsional twisted polymer actuators

Several configurations for torsional polymer actuators have been studied [34, 2, 1]. In this thesis, I present single monofilament and parallel STPA configurations. Both configurations were fabricated in a similar way to previous works investigating torsional and linear actuation of TPAs [34]. The single monofilament configuration consists of a straight twisted monofilament and the parallel STPA is created by gently twisting the three single twisted monofilaments around each other.

Figure 4.2 shows the tools that were used during the fabrication process. Figure 4.2(a) shows the fabrication tool for a monofilament STPA. It consists of two towers connected by an aluminum rail. The first tower is fixed at one end of the rail with a hook attached at the center, while the second tower is free to move along the rail, with another hook attached at its center and aligned with the hook on the rigid tower. These hooks are free to spin but can also be locked with a nut. During fabrication, a straight desiccated precursor monofilament is attached in between the hooks. Precursor monofilaments were desiccated by the same method as explained in Section 3.2.1. Each hook rotates in opposite directions, producing the twist and also contraction of the sample. Contraction is allowed by the movable tower, which progressively moves through the rail as the sample is twisted, and subsequently contracts. A tensile force can be applied in order to facilitate this operation and keep the monofillament free of coiling by adding a weight to the free-moving tower.

Figure 4.2(b) shows the fabrication tool for a parallel STPA, where the only difference from the previous tool is that three hooks are set in the rigid tower, forming a equilateral triangle whose center is aligned with the movable tower hook. If the three hooks are spun clockwise, the single hook will be twisted counterclockwise, and the parallel STPA will start forming at the beginning of the single hook. To keep the parallel STPA from becoming a TCPA, more twists were inserted on the three hooks on the rigid tower than on the single hook on the movable tower. In this work, the ratio of twists was 3:1. Images of the resulting STPA and parallel STPA are shown in Figure 4.1.

After inserting the desired number of twists on the STPA (i.e. the number of twists on each of the three hooks for the parallel STPA), a specific pitch angle, $\alpha$, is attained (see Figure 2.1(a) from Section 2). The pitch angle with respect the radial

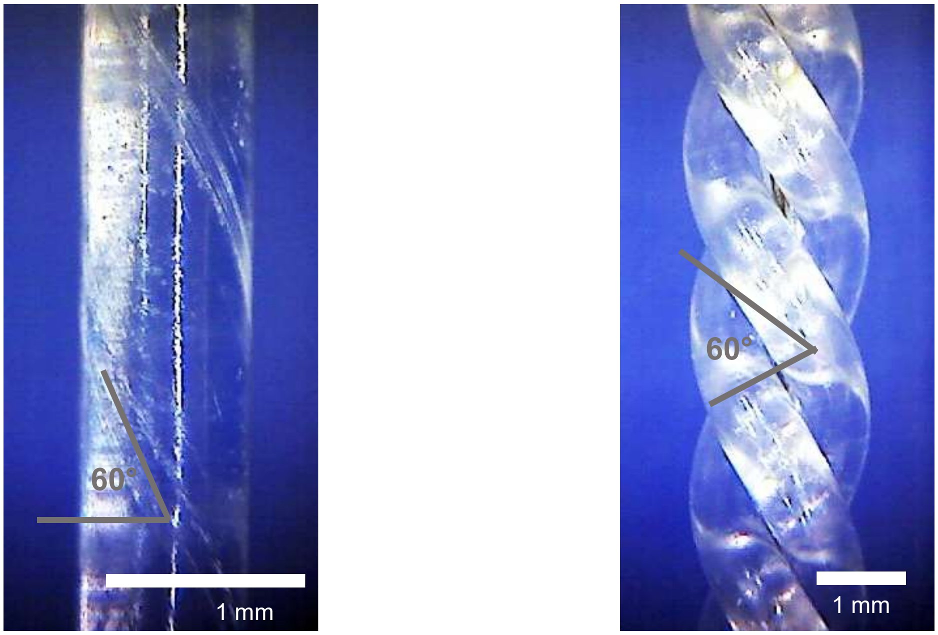

(a) (b)

Figure 4.1: (a) 60° pitch angle monofilament STPA; (b) 60° pitch angle parallel STPA

axis can be calculated using

$$\alpha = (90^\circ - \tan^{-1} \pi D T) \tag{4.1}$$

where $D$ is the diameter of the monofilament and $T$ the number of inserted twists per unit length.

Based on experimental results, it was believed that the greater the number of inserted twists in a STPA, the higher the performance [1, 3, 34]. The maximum number of twists is limited by the shear strength and tensile strength of the material. However, it was shown in STPA actuation modeling that the maximum torsional

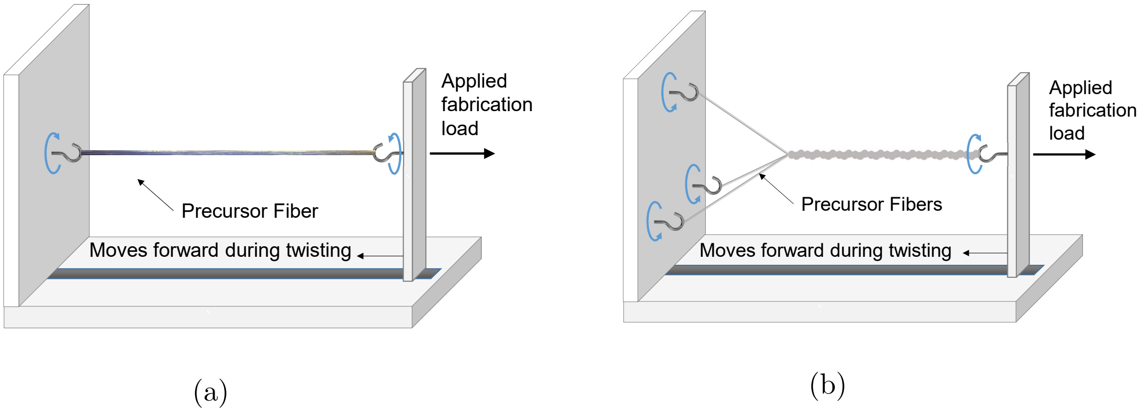

Figure 4.2: (a) Fabrication tool for a single twisted polymer actuator; (b) fabrication tool for a parallel twisted polymer actuator.

actuation was given for a pitch angle of 26.8° [43], which means that the smallest pitch angle does not necessarily produce the highest actuation results. For nylon 6,6 used in this work, it was found that pitch angles of 0 - 47° were achievable with this fabrication process. Once the fabrication process is complete, STPA is tightened by applying load to the movable tower in order to prepare for the annealing process. The fabrication tool along with the STPA is put in an oven at a temperature of 120°C for 20 minutes. This annealing temperature and time was used in other fabrication processes [3], and thought to be adequate because the samples is exposed enough time to an annealing temperature between the melting and glass transition temperature of the material, which allows the new microstructure rearrangement. The sample then is cooled down to room temperature by free convention. This thermal treatment causes the new given orientation of the fibers to be permanently fixed by removing the internal stresses at the fabricated pitch angle. Finally, the sample is cut to the desired length and placed back in desiccant.

## 4.2 Experimental setups for thermal actuation of TPAs

Two different setups were designed and built for the acquisition of torsional actuation data of a STPAs under different mechanical loading conditions. The first was a setup for free torsional actuation and the second one was for actuation under a constant torque.

### 4.2.1 Free torsional actuation setup

A TA Instruments Hybrid Discovery Rheometer 2 (HR-2) was used to measure the torsional actuation of a STPA under no load. The temperature was manually controlled by the Sparkfun Electronics 303D heat gun controller and the average temperature of STPAs was recorded by the FLIR A300-Series thermal camera with an IR 10 mm focal lens.

Figure 4.3 shows a diagram of the HR-2 along with a zoomed photography of the torsional accessory used to clamp the 2-cm long sample in place. While the heat gun applies the temperature load approximately linearly, the temperature and the free torsional displacement of the sample are recorded by the thermal camera and the load cell of the HR-2, respectively.

### 4.2.2 Isotonic torsional load actuation setup

In axial and torsional actuation, it has been shown that a preload helps to bring these actuators back to the initial position [1]. Therefore, an experimental setup was built to test the STPAs actuation under a constant torque.

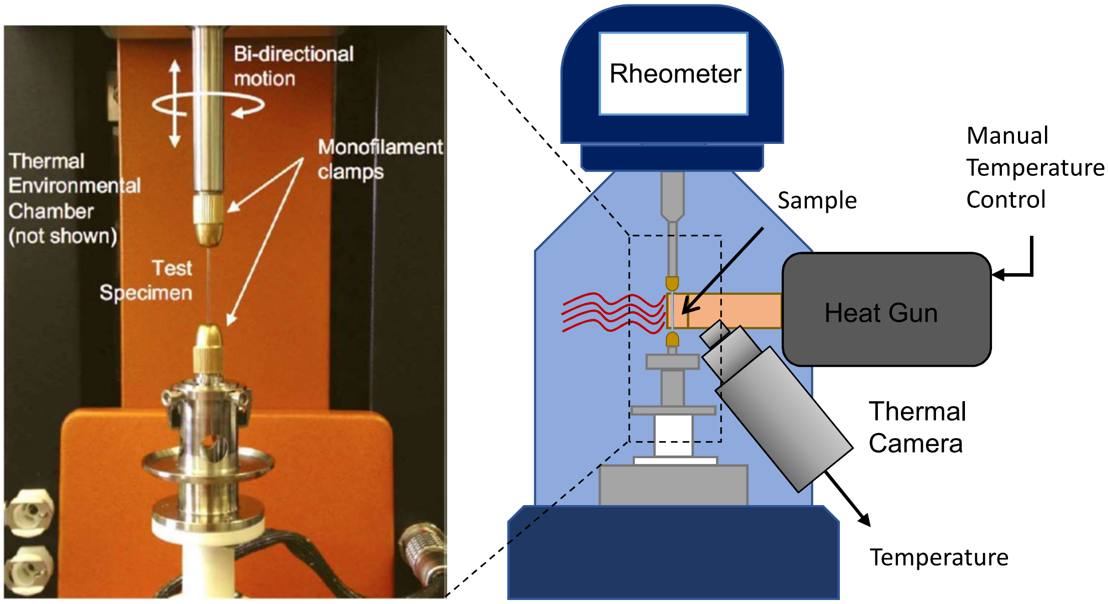

Figure 4.3: Rheometer and Torsional Accessory used for free torsion actuation measurements.

Figure 4.4 shows the components of this setup: a 3D printed frame, torque spool, clamp, weight, thermocouple, and a heat gun. Figure 4.4(b) displays how the STPA is clamped at the right end and glued into the hollow of the torque spool. The spool can rotate free by a pair of ball bearings. A constant torque is produced by a weight that hangs from the 6 mm diameter torque spool on a thin steel wire.

The changes in position of the mass were measured using the Polytec OVF-5000/OVF-534 vibrometer controller and sensor unit, along with DD-900 Digital Displacement Decoder unit. The obtained output of this system was given in voltage, which was linearly related to a change of position of the focused object (0.01 $\mu$m/V

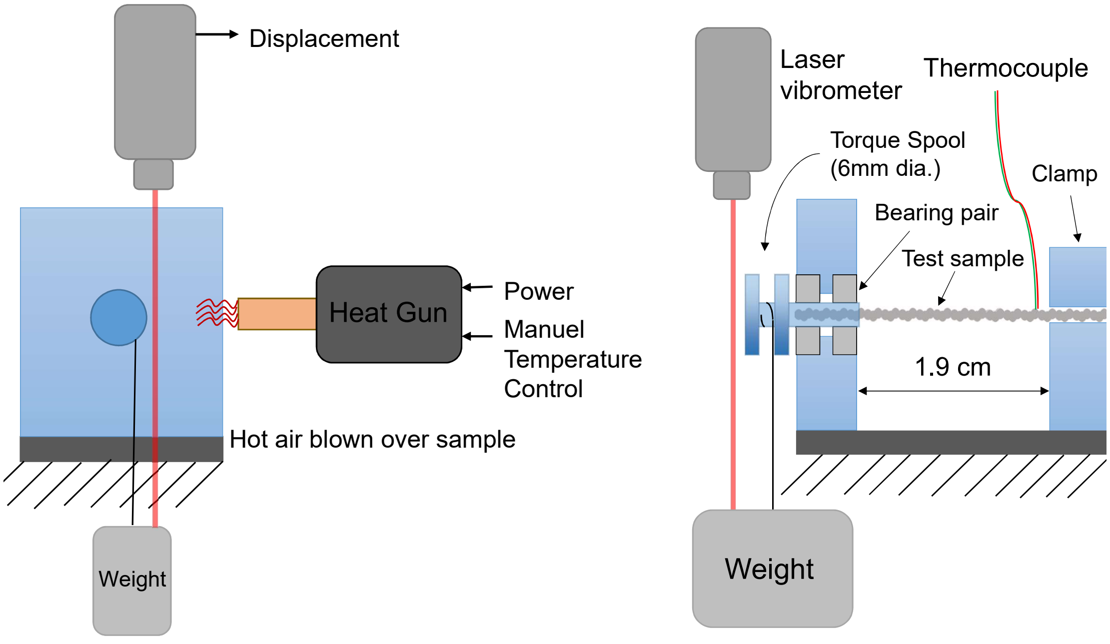

(a) (b)

Figure 4.4: Isotonic experimental testing rig for measuring actuation stroke under thermal loading; (a) front view; (b) side view.

and a slow track filter). Additionally, the sample's temperature was measured using K-type thermocouples embedded within the test sample for the parallel STPAs and taped for the monofilament STPAs. Note that this test was performed before the thermal camera was obtained, but that may be a preferable way to measure temperature in future isotonic actuation tests. The temperature was controlled manually using the Sparkfun Electronics 303D heat gun controller as shown in Figure 4.4(a). After heating to the desired temperature, the heat gun was removed and the sample was cooled under free convection to room temperature. The temperature and displacement were recorded by a National Instruments PXI-6361 multifunction data acquisition card.

## 4.3 Experimental methods and actuation results

### 4.3.1 Free torsion actuation

For the free torsion actuation test, no thermal pre-cycling was conducted before the test in order to observed first cycle effects during torsional actuation. However, a total of four thermal cycles were conducted between room temperature and approximately 100°C. The first cycle of the test was longer than the subsequent cycles because this first cycle was used as pre-cycle for the actuator. This first cycle consisted of a heating ramp of approximately 30 minutes followed by a cooling ramp of 20 minutes. After this pre-cycle, three more cycles were applied to the sample with approximately linear heating ramps lasting two minutes, with a recovery time of 20 minutes. Additionally, constant axial force of 0.1 N in tension was applied to the sample in the HR-2 to guarantee that the sample did not buckle.

Figure 4.5 and 4.6 show the change in twist and contraction produced by two STPAs with outer radius pitch angles of 75° and 54°, respectively. As expected, first cycle effects are present; the initial change in twist and contraction are considerably larger in the first cycle than subsequent cycles. Additionally, in subsequents cycles total recovery does not occur and no convergence is observed. Convergence of actuation has been studied by Haines et al. [1], where a coiled nylon 6,6 muscle was exposed over a million 1 Hz's cycles under a mechanical load of 22 MPa. The creep was bellow 2 % over 1.2 million cycles and change in stroke was assumed negligible. Even though the configurations of both actuators are different is expected to find the same convergence after a specific number of cycle, where high frequency will lead to

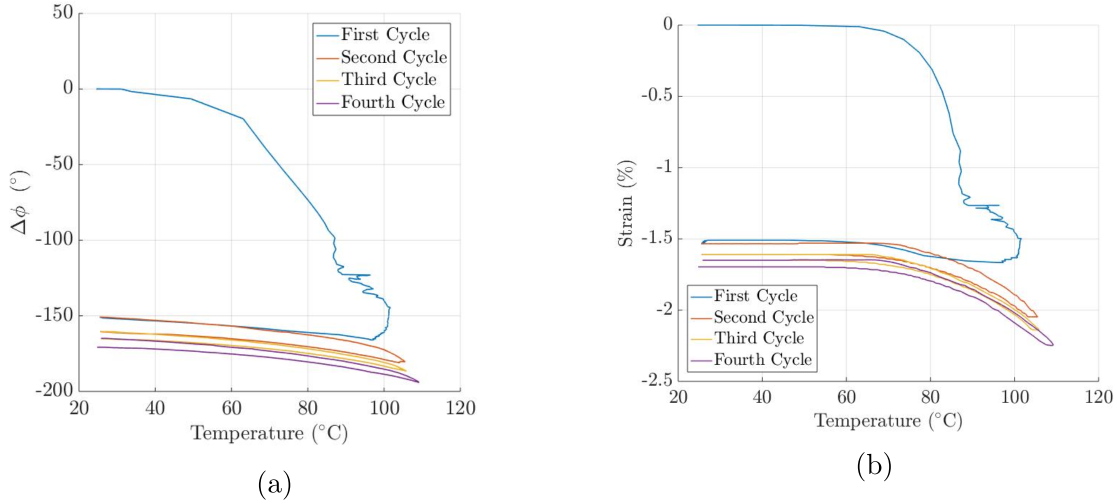

(a)

(b)

Figure 4.5: Experimental results for a 75° pitch angle STPA; (a) change in twist for the five first cycles; (b) contraction for the five first cycles.

faster convergence due to the shorter recovery time. Furthermore, hysteresis is also present, which is expected as many of the studied properties of this material show a viscoelastic response. Figures 4.5(a) and 4.6(a) show the change in twist results for the 75° and 54° pitch angle STPAs, respectively. As mentioned, a first cycle effect produces a large torsional displacement for only one cycle, approximately 400% of the final change in twist for both actuators. Then actuation results start repeating with the same actuation behavior; however, the actuation does not seem to converge to a stable actuation cycle. Again, it is thought that a higher number of cycles might be needed for total convergence [1]. The change in twist for the last cycle is 29° for the STPA with pitch angle of 75°, while the change in twist is 66° for the last cycle of the STPA with pitch angle of 54°; thus, by decreasing the pitch angle 21° (inserting more twist in the monofilament), the actuation increases by 128%.

Figures 4.5(b) and 4.6(b) show the contraction for the 75° and 54° pitch angle

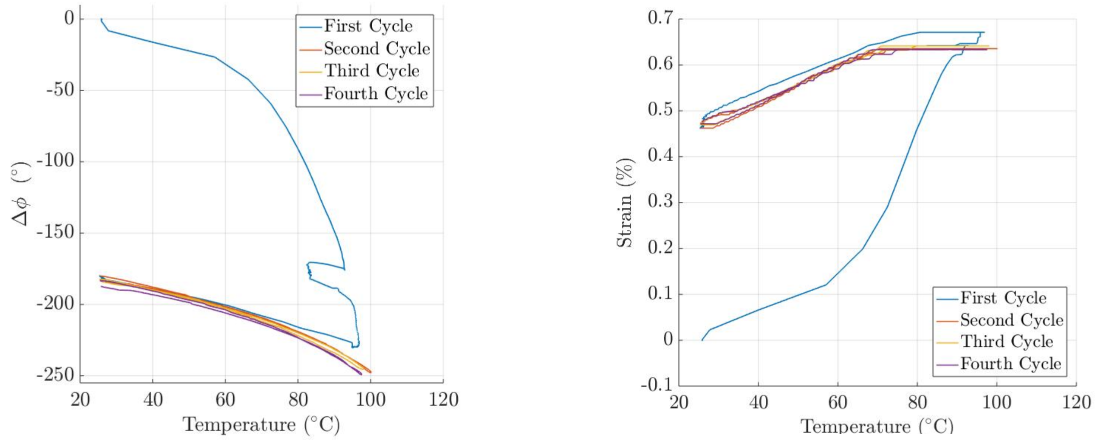

(a)

(b)

Figure 4.6: Experimental results for a 54° pitch angle STPA; (a) change in twist for the five first cycles; (b) contraction for the five first cycles.

STPAs, respectively. After the first cycle, the rest of the cycles start converging, but full convergence is not shown. The thermal contraction in Figure 4.5(b) presents similarities with the axial thermal contraction of the precursor monofilament shown in Figure 3.20(b), where the axial contraction remains constant below temperatures close to 60°C and quickly increases for temperatures above 60°C. This similarity between the precursor monofilament and the 75° pitch angle STPA is explained by the small differences in the orientations of the fibers. Figure 4.6(b) shows how the STPA with more initial twist extends up to a temperature of 75°C above which the STPA's length does not significally change. This result is due to the new highly twisted orientation of the fibers, where there is more contribution to change in length from radial thermal expansion, thus causing the STPA to expand.

### 4.3.2 Actuation under Torsional Load

Actuation tests under isotonic torsional loads were performed similarly to the free torsion test, where no thermal pre-cycling was conducted before the test, but several cycles were run to observe first cycle effects. A total of five cycles were conducted for each configuration (parallel and monofilament STPAs) with a pitch angle of 60°, under high and low torque for each, while measuring actuation angles as a function of temperature.

The temperature was ramped between room temperature and approximately 100°C in approximately 20 seconds, while the cooling periods lasted approximately 10 minutes, due to the slow cooling process under free convection.

Figure 4.7 displays the actuation results for a single monofilament STPA under two constant torsional loads: a low load 0.883 N-mm (Figure 4.7(a)) and a high load of 2.94 N-mm (Figure 4.7(b)). Similar experimental results are plotted in Figure 4.8 for the parallel configuration under torque loads three times higher than for the single monofilament STPA test (2.94 N-mm and 8.33 N-mm), since the parallel configuration used three twisted monofilaments braided between each other.

During the first cycle for the low loading tests in the monofilament and parallel STPAs, results show large actuation angles with low recovery. Figure 4.7(a) shows a change in twist during the first actuation cycle of approximately 28° with a recovery of 8°, and similarly, Figure 4.8(a) shows a similar behavior, where the first cycle reaches up to 34° and has a recovery of 12°. After the first cycle, the actuation results are more consistent. A change in twist of 7.5° were found for the monofilament STPA and 12° for the parallel STPA under low mechanical loading for the last cycle.

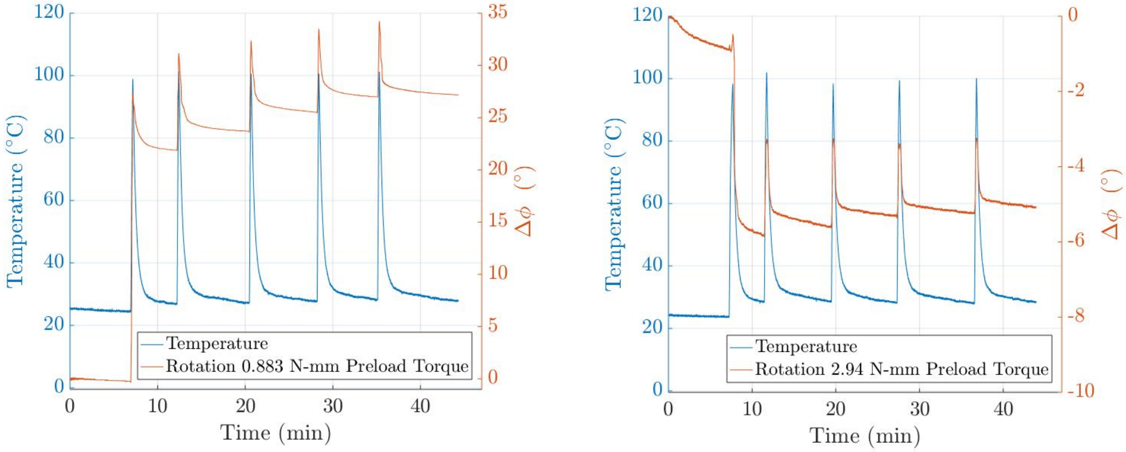

(a) (b)

Figure 4.7: Angular displacement and temperature as a function of time for five cycles of actuation; (a) torsional load of 0.833 N-mm; (b) torsional load of 2.94 N-mm.

For the higher load experiments (Figures 4.7(b) and 4.8(b)), a similar first cycle effect is observed; however, the samples relax under the mechanical and thermal load during this cycle, causing this material to gain positive change in twist.

Figures 4.7(b) and 4.8(b) show shear stress relaxation for the first seven minutes at room temperature, which is expected because of the time dependency of the shear modulus (Chapter 3). After ramping the temperature, the material actuates; however, the increase in temperature speeds up the shear relaxation since the shear modulus decreases (Figure 3.13(b)), and the change in twist is more positive for the first cycle. A change in twist of 2.3° was found for the monofilament STPA and a change in twist 8.8° was found for the parallel STPA under high mechanical loading.

Figures 4.9(a) and 4.9(b) show the change in twist as a function of temperature of all actuation tests. In these results, nearly total recovery is observed in the parallel

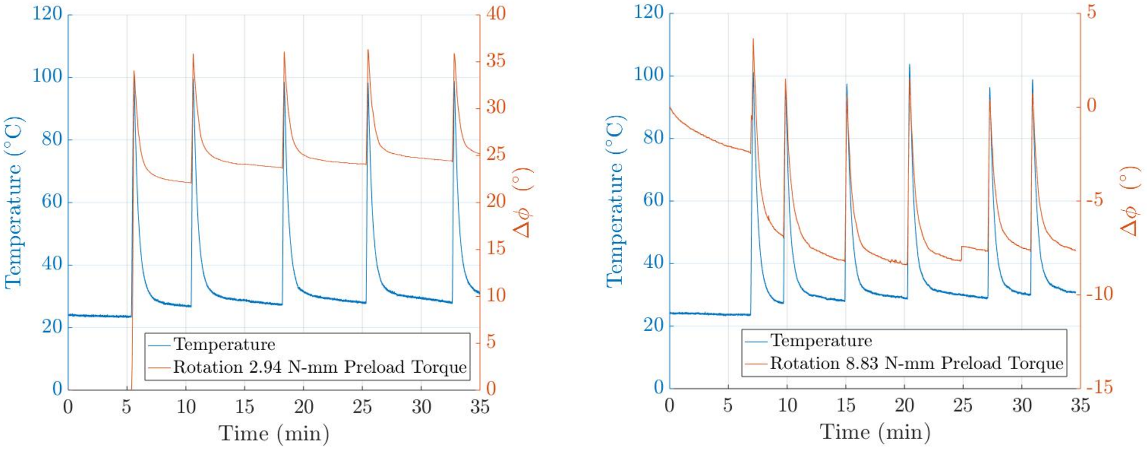

(a) (b)

Figure 4.8: Angular displacement and temperature as a function of time for five cycles of actuation; (a) torsional load of 2.94 N-mm; (b) torsional load of 8.83 N-mm.

configuration after the first cycle for both loads; however, the monofilament STPA shows only partial recovery for both loads. To yield convergence a higher number of cycles in the order of millions should be conducted, as shown by Haines et al. [1]. In addition, hysteresis is present in all of these cycles due to viscoelastic effects of the material. This actuation test shows a stronger hysteretic behavior than the one shown for the free torsion test. This increase of hysteresis is due to the applied mechanical load, which leads the material to experience greater viscoelastic responses.

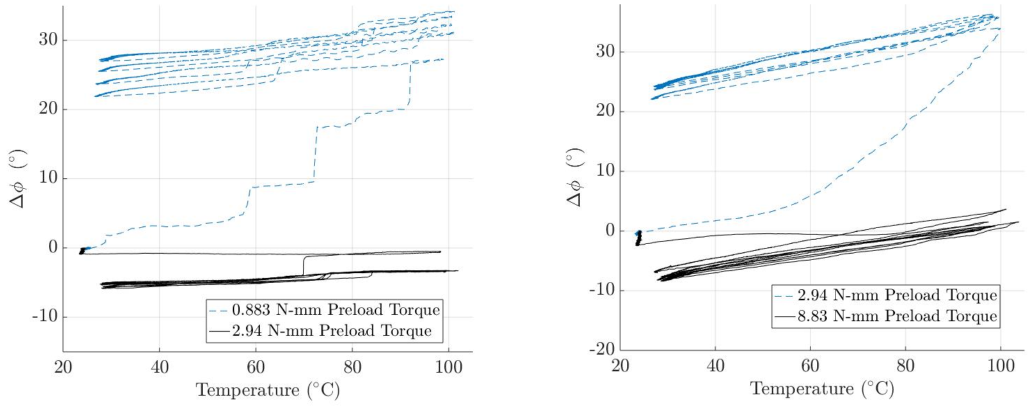

(a) (b)

Figure 4.9: Angular displacement versus temperature for five cycles of actuation; (a) monofilament STPA; (b) parallel STPA.

## Chapter 5

# Conclusions

### 5.1 Contributions

In this work, I show experimental setups and methods for the collection of mechanical and thermal properties for drawn polymer monofilament, specifically, I acquired viscoelastic, and thermal properties of Berkley Trilene® Big Game™ nylon 6,6. I show that many of the mechanical and thermal properties of the precursor monofilament are time-dependent and also present a first cycle effect. These are two vital considerations for future modeling of TPAs. Actuation results will not be consistent until a stable actuation state is achieved and viscoelastic effect disappear. Changes in the material properties due to viscoelastic effects have been shown to occur very quickly in the first minutes and tend to yield steady state after about 20 minutes. With the goal to model this time-dependencies, the parallel Zener model with two dash-spring elements seems to be the viscoelastic model that generally captures the response of this material best. Table 5.1 shows each of the properties measured in

Table 5.1: Time, temperature, and first cycle effect dependence for the mechanical and thermal properties of the precursor monofilament

| **Properties of the precursor monofilament** | **Time dependent** | **Temperature dependent** | **First cycle effect** |
|---|---|---|---|
| $E_1$ | Yes | Yes | Yes |
| $E_2$ | Yes | Unknown | Yes |
| $G_{12}$ | Unknown | Unknown | Yes |
| $\nu_{12}$ | Yes | Yes | Yes |
| $\alpha_{11}^T$ | Minimal | Yes | Yes |
| $\alpha_{22}^T$ | No | Yes | Yes |

this work and the extent to which show time, temperature, and first cycles effects dependency.

Mechanical properties were found to be dependent on temperature. Changes in temperature not only change the magnitude of mechanical properties but increase viscous effects in the precursor monofilament, making the variables time and temperature related. Table 3.1 shows mathematical expression for the precursor monofilament properties with respect the time and temperature, which can be used as model inputs.

In addition to measuring material parameter of precursor monofilaments, I also fabricated STPA and measured their actuation (with and without torsional load) response. The isotonic torsional actuation tests were performed for two different configurations: single monofilament and parallel STPAs. This data can be used for comparing future actuation models with experimental results. Similar to the precursor monofilaments, STPAs showed first cycle effects. Time dependency was also seen in STPAs in the hysteresis of the stroke-temperature response.

The results of the studied mechanical and thermal properties as well as actuation results have implications for the use of TPAs. Changes in actuation as a function of time and number of cycles are critical factors in the implementation of STPAs. STPAs are expected to actuate on the order of seconds, so viscoelastic effect can be neglected and simpler modeling applies. Moreover depending on the time between cycles, TPAs may need to be continuously precycled to give consistent actuation results. Furthermore, investigation of other drawn polymers can be conducted to see if they present the same characteristics.

## 5.2 Future Work

The properties of the precursor monofilament in this study have been found to be strongly dependent on variables, such as humidity, time, temperature, and first cycles effect. In future works, further testing of the material properties may be beneficial for the characterization of the precursor monofilament. With the goal to obtaining a better understanding of the first cycle effect, experimental testing for the mechanical properties may be conducted under different mechanical loads for either just the first or all cycles. This would be useful because the Mullin's effect is often associated with the maximum prior load, and so it would be important to see if that is true for drawn polymer monofilaments. From this experiment, a new preparation protocol for the TPAs may be obtained to eliminate the first cycle effect.

Further testing can be also conducted in order to characterize the time-dependency of the precursor monofilament as a function of temperature, these experiments may be achieved by dynamic mechanical analysis. Similarly, testing the viscoelastic properties for a range of frequencies will help to identify at which frequency, hysteresis is minimize, which would be ideal for actuation.

Collecting data of the precursor monofilamente properties as a function of different moisture levels will help to obtained a better characterization of the material and actuation modeling, for applications where moisture concentration levels can not be controlled.

More work is needed on actuation modeling of STPAs and TCPAs, as the Shafer et al. [3] model does not include internal stresses or external mechanical load and the Yang et al. [14] model requires transformation of properties that leads to complex expressions. Once new model are developed, it will be interesting to see how well the precursor monofilament properties predict actuation.

Finally, future work on applications of TPAs will be important to translate the knowledge gain this work on technologies. Under the conditions of time and first cycle effect dependencies, actuation will be limited to specific cases where actuation performs quickly and viscous effects can be neglected. In addition, TPAs maybe good for one-impulse actuators where the actuator is designed to actuate only once, then the first cycle effect is no longer a parameter to take into account. More complex applications can be designed with of a complementary feedback control system but that may be cumbersome.

# Bibliography

[1] C. S. Haines, M. D. Lima, N. Li, G. M. Spinks, J. Foroughi, J. D. Madden, S. H. Kim, S. Fang, M. J. de Andrade, F. Göktepe, *et al.*, "Artificial muscles from fishing line and sewing thread," *Science*, vol. 343, no. 6173, pp. 868–872, 2014.

[2] S. Aziz, S. Naficy, J. Foroughi, H. R. Brown, and G. M. Spinks, "Controlled and scalable torsional actuation of twisted nylon 6 fiber," *Journal of Polymer Science Part B: Polymer Physics*, vol. 54, no. 13, pp. 1278–1286, 2016.

[3] M. W. Shafer, H. P. Feigenbaum, D. Pugh, and M. Fisher, "First steps in modeling thermal actuation of twisted polymer actuators using virgin material properties," in *ASME 2016 Conference on Smart Materials, Adaptive Structures and Intelligent Systems*, pp. V002T06A017–V002T06A017, American Society of Mechanical Engineers, 2016.

[4] D. Prevorsek, P. Harget, R. Sharma, and A. Reimschuessel, "Nylon 6 fibers: changes in structure between moderate and high draw ratios," *Journal of Macromolecular Science, Part B: Physics*, vol. 8, no. 1-2, pp. 127–156, 1973.

[5] J. A. Peter, K. A. Jayanth, M. A. Christopher, and A. Kari, "Shape memory al-

loy tini actuators for twist control of smart wing designs," *Proc.SPIE*, vol. 2717, pp. 1 – 6, 1996.

[6] J. Foroughi, G. Spinks, G. Wallace, J. Oh, M. Kozlov, S. Fang, T. Mirfakhrai, J. Madden, M. Kyoon Shin, S. J. Kim, and R. Baughman, "Torsional carbon nanotube artificial muscles," vol. 334, pp. 494–7, 10 2011.

[7] L. Wu and Y. Tadesse, "Musculoskeletal system for bio-inspired robotic systems based on ball and socket joints," *International Mechanical Engineering Congress and Exposition*, vol. 4A, pp. 11–16, 2016.

[8] T. Mirfakhrai, J. Oh, M. Kozlov, E. C. W. Fok, M. Zhang, S. Fang, R. H. Baughman, and J. D. W. Madden, "Electrochemical actuation of carbon nanotube yarns," *Smart Materials and Structures*, vol. 16, no. 2, p. S243, 2007.

[9] H. Tobushi, S. Hayasi, and S. Kojima, "Mechanical properties of shape memory polymer of polyurethane series : Basic characteristics of stress-strain-temperature relationship," *JSME international journal. Ser. 1, Solid mechanics, strength of materials*, vol. 35, no. 3, pp. 296–302, 1992.

[10] Y. Bar-Cohen, *Electroactive Polymer (EAP) Actuators as Artificial Muscles: Reality, Potential, and Challenges.* Press Monographs, SPIE Press, 2001.

[11] A. Arjun, L. Saharan, and Y. Tadesse, "Design of a 3d printed hand prosthesis actuated by nylon 6-6 polymer based artificial muscles," pp. 910–915, Aug 2016.

[12] F. Karami and Y. Tadesse, "Modeling of twisted and coiled polymer (tcp) muscle

based on phenomenological approach," *Smart Materials and Structures*, vol. 26, no. 12, pp. 1–12, 2017.

[13] S. Sharafi and G. Li, "A mutliscale approach for modeling actuation response of polymeric artificial muscle," *Soft Matter*, no. 12, pp. 1–18, 2015.

[14] Q. Yang and G. Li, "A top-down multi-scale modeling for actuation response of polymeric artificial muscles," *Journal of the Mechanics and Physics of Solids*, vol. 92, no. 12, pp. 237–259, 2016.

[15] S. L. Hunter, I.W., "A comparison of muscle with artificial actuators," *Technical Digest of the IEEE Solid-State Sensor and Actuator Workshop*, p. 178185, 1992.

[16] D. J.Leo, *Engineering Analysis of Smart Material Systems.* 2008.

[17] I. Chopra and J. Sirohi, *Smart Structures Theory.* Cambridge Aerospace Series, Cambridge University Press, 2013.

[18] I. Hunter, J. Hollerbach, S. Lafontaine, and P. Hunter, "Fast reversible niti fibers for use in microrobotics," p. 166170, 1991.

[19] S. Kothera, M. Jangid, J. Sirohi, and N. Wereley, "Experimental characterization and static modeling of mckibben actuators," *Journal of Mechanical Design*, vol. 122, p. 751, 08 2009.

[20] C. S. Haines, N. Li, G. M. Spinks, A. E. Aliev, J. Di, and R. H. Baughman, "New twist on artificial muscles," *Proceedings of the National Academy of Sciences*, vol. 113, no. 42, pp. 11709–11716, 2016.

[21] M. Hiraoka, K. Nakamura, H. A. K. Asai, Y. Kaneko, S. W. John, K. Tagashira, and A. Omote, “Power-efficient low-temperature woven coiled fibre actuator for wearable applications,” *Scientific reports*, no. 6:36358, pp. 1–9, 2016.

[22] A. E. Chapman, “The mechanical properties of human muscle,” *Exercise and Sport Sciences Reviews*, vol. 13, 2009.

[23] H. Y. Jun, O. K. Rediniotis, and D. C. Lagoudas, “Development of a fuel-powered shape memory alloy actuator system: I. numerical analysis,” *Smart Materials and Structures*, vol. 16, no. 1, p. S81, 2007.

[24] R. D. Bassem Andrawes, “Effect of ambient temperature on the performance of shape memory alloy seismic devices,” *Proc.SPIE*, vol. 5764, pp. 5764 – 5764 – 9, 2005.

[25] R. Mohr, K. Kratz, T. Weigel, M. Lucka-Gabor, M. Moneke, and A. Lendlein, “Initiation of shape-memory effect by inductive heating of magnetic nanoparticles in thermoplastic polymers,” *Proceedings of the National Academy of Sciences*, vol. 103, no. 10, pp. 3540–3545, 2006.

[26] G. K. Klute, J. M. Czerniecki, and B. Hannaford, “Mckibben artificial muscles: pneumatic actuators with biomechanical intelligence,” pp. 221–226, Sept 1999.

[27] B. Tondu, “Modelling of the mckibben artificial muscle: A review,” *Journal of Intelligent Material Systems and Structures*, vol. 23, no. 3, pp. 225–253, 2012.

[28] J. Madden and S. Kianzad, “Twisted lines: Artificial muscle and advanced

instruments can be formed from nylon threads and fabric.," *Pulse, IEEE*, vol. 6, no. 1, pp. 32–35, 2015.

[29] M. Baghani, "Analytical study on torsion of shape-memory-polymer prismatic bars with rectangular cross-sections," *International Journal of Engineering Science*, vol. 76, pp. 1 – 11, 2014.

[30] Y. Fang, T. J. Pence, and X. Tan, "Fiber-directed conjugated-polymer torsional actuator: Nonlinear elasticity modeling and experimental validation," *IEEE/ASME Transactions on Mechatronics*, vol. 16, pp. 656–664, Aug 2011.

[31] S. Sanan, P. Lynn, and S. T. Griffith, "Pneumatic torsional actuators for inflatable robots," *Journal of Mechanisms and Robotics*, vol. 6, April 2014.

[32] K. Chun, K. S. Hyeong, S. M. Kyoon, K. C. Hoon, J. Park, K. Y. Tae, G. M. Spinks, M. D. Lima, C. S. Haines, R. H. Baughman, and K. S. Jeong, "Hybrid carbon nanotube yarn artificial muscle inspired by spider dragline silk," vol. 5, pp. 494–7, 02 2014.

[33] D. Suh, T. K. Truong, D. G. Suh, and S. C. Lim, "Torsional actuator powered by environmental energy harvesting from diurnal temperature variation," *ACS Sustainable Chemistry & Engineering*, vol. 4, no. 12, pp. 6647–6652, 2016.

[34] M. Shafer, H. Feigenbaum, and D. Higueras Ruiz, "A novel biomimetic torsional actuator design using twisted polymer actuators," *Smart Materials, Adaptive Structures and Intelligent Systems*, vol. 1, pp. 1–7, 2017.

[35] D. C. Prevorsek, P. J. Harget, K. Sharma, and A. C. Reimschuessel, “Nylon 6 fibers: Changes in structure between moderate and high draw ratios,” *Journal of Macromolecular Science*, vol. Part B,8:1-2, pp. 127–156, 2016.

[36] D. C. Prevorsek, Y. D. Kwon, and R. K. Sharma, “Nylon 6 fibers: Changes in structure between moderate and high draw ratios,” *Journal of Materials Science*, vol. 12, pp. 2310–2328, 1977.

[37] C. Choy, F. Chen, and K. Young, “Negative thermal expansion in oriented crystalline polymers,” *Journal of Polymer Science: Polymer Physics Edition*, vol. 19, no. 2, pp. 335–352, 1981.

[38] J. Elad and J. Schultz, “Microstructural rearrangement during heat treatment of drawn nylon 66 fiber,” *Journal of Polymer Science: Polymer Physics Edition*, vol. 22, no. 5, pp. 781–792, 1984.

[39] V. Bukoek and D. C. Prevorsek, “Model of nylon 6 fibers microstructure microfibrillar model or “swiss-cheese” model?,” *International journal of polymeric materials*, vol. 47, no. 4, pp. 569–592, 2000.

[40] J. A. Bruno, N. L. Allan, T. H. Barron, and A. D. Turner, “Thermal expansion of polymers: Mechanisms in orthorhombic polyethylene,” *Physical Review B*, vol. 58, no. 13, pp. 8416–8427, 1998.

[41] W. Hilber, “Stimulus-active polymer actuators for next-generation microfluidic devices,” *Applied Physics A*, vol. 122, p. 751, Jul 2016.

[42] Y. Almubarak and Y. Tadesse, "Twisted and coiled polymer (tcp) muscles embedded in silicone elastomer for use in soft robot," 04 2017.

[43] A. M. Swartz, D. R. Higueras Ruiz, H. P. Feigenbaum, M. W. Shafer, , and C. C. Browder, "Experimental characterization and model predictions for twisted polymer actuators in free torsion," *Smart materials and structures, Pending for publishing.*

[44] R. F. Gibson, *Principles of composite material mechanics.*

[45] Y. C. Fung, "Foundations of solid mechanics," *Prentice-Hall.*

[46] V. A. Alvarez, A. N. Fraga, and A. Vazquez, "Effects of the moisture and fiber content on the mechanical properties of biodegradable polymersisal fiber biocomposites," *Journal of Applied Polymer Science*, vol. 91, no. 6, pp. 4007–4016.

[47] J. Diani, B. Fayolle, and P. Gilormini, "A review on the mullins effect," *European Polymer Journal*, vol. 45, no. 3, pp. 601 – 612, 2009.

[48] X. Li, Y. Wei, Q. Feng, and R. K. Luo, "Mechanical behavior of nylon 66 tyre cord under monotonic and cyclic extension: Experiments and constitutive modeling," *Fibers and Polymers*, vol. 18, no. 3, pp. 542–548, 2017.

[49] A. Lendlein and R. Langer, "Biodegradable, elastic shape-memory polymers for potential biomedical applications," *Science*, vol. 296, no. 5573, pp. 1673–1676, 2002.

[50] I. M. Ward and J. Sweeney, "Mechanical properties of solid polymers," *John Wiley and Sons, Ltd*, vol. 3, 2012.

[51] P. Plastics, "Mechanical properties of plastic materials,"